**Title: Chickpea NCR13 disulfide cross-linking variants exhibit profound differences in antifungal activity and modes of action**

**Authors:** James Godwin[a,1], Arnaud Thierry Djami-Tchatchou[a,1], Siva L. S. Velivelli[a], Meenakshi Tetorya[a], Raviraj Kalunke[a], Ambika Pokhrel[a], Mowei Zhou[c,2], Garry W. Buchko[c,d], Kirk J. Czymmek[a,b], and Dilip M. Shah[a,3]

**Author Affiliations:**

[a]Donald Danforth Plant Science Center, St Louis, MO. 63132, USA

[b]Advanced Bioimaging Laboratory, Donald Danforth Plant Science Center, St Louis, MO. 63132, USA

[c]Earth and Biological Sciences Directorate, Pacific Northwest National Laboratory, Richland, WA 99354, USA

[d]School of Molecular Biosciences, Washington State University, Pullman, WA 99164, USA

1. These authors contributed equally to the manuscript.

2. Current address: Department of Chemistry, Zhejiang University, 866 Yuhangtang Road, Hangzhou, Zhejiang 310058, China

3. **Corresponding Author:** (dshah@danforthcenter.org)

**Abstract**

Cationic nodule-specific cysteine-rich (NCR) peptides of nitrogen-fixing legume plants exhibit antifungal activity and can be repurposed for development as biofungicides. Chickpea NCR13 is a highly cationic peptide with six cysteines forming three disulfide bonds. Expression of NCR13 in *Pichia pastoris* resulted in formation of two peptide folding variants, NCR13_PFV1 and NCR13_PFV2, that differed in the pairing of two out of three disulfide bonds despite having an identical amino acid sequence. The NMR structure of each PFV revealed a unique three-dimensional fold with the PFV1 structure being more compact but less dynamic. PFV1 and PFV2 differed profoundly in the potency of antifungal activity and their multi-faceted modes of action (MoA). PFV1 showed significantly faster fungal cell-permeabilizing and cell entry capabilities and greater stability once inside the fungal cells. PFV1 was more effective in binding to fungal ribosomal RNA and inhibiting protein translation *in vitro*. When sprayed on pepper and tomato plants, PFV1 was more effective in controlling the gray mold disease caused by *Botrytis cinerea*. Our work highlights the significant impact of disulfide pairing on the antifungal activity and MoA of NCR13 and provides structural framework for design of novel, potent antifungal peptides for agricultural use.

## Introduction

The management of fungal diseases using chemical fungicides is one of the mainstays of modern agriculture. Unfortunately, modern fungicides that have a single site mode of action (MoA) are losing their effectiveness owing to an increase in development of fungal resistance (McLaughlin et al., 2023). A major limitation in fungicide development is finding molecules with novel structures and multi-site MoA to mitigate evolution of resistance.

Plants express many antimicrobial peptides that are vital components of the innate immune system and act as a first line of defense against bacterial and fungal pathogens (Dos Santos-Silva et al., 2020; Goyal & Mattoo, 2014). Moreover, plants express a multitude of cationic antifungal peptides differing in structure and sequence (van der Weerden et al., 2013). They are versatile, have large sequence space, and can be tuned for broad-spectrum antifungal activity against plant fungal pathogens. Thus, cationic antimicrobial peptides represent promising templates for a new generation of fungicides with broad action against fungal pathogens (Lobo & Boto, 2022).

Several antifungal peptides expressed in plants are cysteine-rich with a characteristic number of cysteine-residues at conserved positions and exhibit high degree of sequence diversity (Tavormina et al., 2015; van der Weerden et al., 2013). Defensins and defensin-like peptides are the best characterized examples of cysteine-rich peptides employed by plants to combat fungal pathogens (Cools et al., 2017; Maroti et al., 2015; Parisi et al., 2019). Legumes of the inverted repeat-lacking clade (IRLC) express many nodule-specific cysteine-rich (NCR) defensin-like peptides that cause differentiation of nitrogen-fixing bacteria to bacteroids. In *Medicago truncatula* and chickpea, terminal differentiation process is orchestrated by 639 and 63 nodule-specific cysteine-rich (NCR) peptides, respectively, with conserved cysteine motifs (Montiel et al., 2017). NCRs cause bacterial genome endoreduplication, changes in transcription and translation,

74 and induction of morphological changes leading to the formation of bacteroids with unique
75 morphology (Kereszt et al., 2018; Kondorosi et al., 2013; Maroti et al., 2015; Mergaert, 2018).
76 Each NCR is synthesized as a precursor protein containing an N-terminal signal peptide and a C-
77 terminal mature peptide. Several NCRs in each legume are cationic with a net charge ranging from
78 +3 to +11 and rich in hydrophobic residues, dual hallmarks of defensin-like antimicrobial peptides
79 (Montiel et al., 2017; Ordogh et al., 2014). Large landscape of natural NCRs from IRLC legumes
80 offers an unprecedented opportunity for discovery of the novel antimicrobial functions in plants.
81 Several NCR peptides exhibiting antibacterial activity against Gram-negative and Gram-positive
82 bacteria have so far been identified (Alhhazmi et al., 2024; Balogh et al., 2014; Farkas et al., 2017;
83 Tiricz et al., 2013). Another report detailed the evaluation of 19 cationic *M. truncatula* NCRs for
84 their ability to inhibit the growth of a human fungal pathogen *Candida albicans*. Of these, nine
85 with a net charge above +9 inhibited the growth of this pathogen at concentrations ranging from
86 1.5 to 10.5 μM (Ordogh et al., 2014). Previously, we reported *M. truncatula* NCR044 having
87 broad-spectrum antifungal activity and multi-faceted MoA. In addition, when sprayed on leaf
88 surfaces of tomato and *Nicotiana benthamiana* plants, NCR044 conferred resistance to the gray
89 mold disease caused by the fungal pathogen *B. cinerea* (Velivelli et al., 2020).

90 NCRs exhibit diverse primary sequences and net charges, with a notable conserved feature
91 being the presence of four or six conserved cysteine residues. These cysteines form intramolecular
92 disulfide bonds which enhance the stability of the peptides (Bulleid & Ellgaard, 2011; Montiel et
93 al., 2017). The influence of cysteines and disulfide cross-linking on the structure and function of
94 *M. truncatula* NCR247 and NCR169, each containing four cysteines, has been previously
95 investigated. Four conserved cysteines and disulfide cross-linking had major influence on the
96 symbiotic activities of NCR247 tested against *Sinorhizobium meliloti* (Haag et al., 2012; Shabab

et al., 2016). NCR169 produced two structurally distinct disulfide variants that exhibited differences in phospholipid binding and antibacterial activity (Isozumi et al., 2021). However, the significance of disulfide cross-linking for the structures, antifungal activity, and MoA of many NCRs remains poorly understood.

In this study, we show that chickpea NCR13, a highly cationic 32 residue peptide, was expressed in *Pichia pastoris* as two structurally unique disulfide variants with an identical amino acid sequence. Interestingly, these two variants exhibited distinct differences in their antifungal potency against economically important plant fungal pathogens. NCR13 disulfide variants displayed notable differences in fungal cell entry, cell permeabilization, stability and MoA against the fungal pathogen *B. cinerea*. While both disulfide variants reduced gray mold disease symptoms by spray application on the leaves of pepper and tomato plants, the NCR13 variant with highly potent *in vitro* antifungal activity was more effective in controlling the disease *in planta*. Our study reveals the remarkable impact of disulfide cross-linking on the structure-activity relationships and MoA of an antifungal defensin-like NCR peptide.

## Results

### Chickpea NCR13 is expressed in *P. pastoris* as two peptide folding variants differing in disulfide pairing

In chickpea, NCR13 is one of 63 predicted NCR peptides expressed only in nodules undergoing differentiation during symbiosis (Montiel et al., 2017; Montiel et al., 2016). NCR13 is a 32-residue peptide with six cysteines predicted to form three disulfide bonds (Figure 1A). Two other homologs of this peptide, NCR07 and NCR15, are also expressed in chickpea nodules with highly conserved cysteine residues (Figure 1A). No other IRLC legumes express NCRs with

120 significant homology to NCR13. NCR13 has 66.6% and 48.4% sequence identity with NCR15
121 and NCR07, respectively, carrying a net charge of +8 and a hydrophobic amino acid content of
122 28%, hallmark features of a potential antifungal peptide (Figure 1B).

123 To investigate the antifungal properties of the NCR13 peptide, it was expressed in a
124 heterologous *Pichia pastoris* system. The peptide was secreted into the growth medium and
125 purified using the cation exchange chromatography. When the NCR13 peptide was subjected to
126 C18 reverse-phase high-performance liquid chromatography (HPLC), we consistently observed
127 two peaks (Figure 1C). In contrast, chemically synthesized NCR13 produced only one peak
128 (Figure 1D). These observations led us to suspect that oxidized NCR13 was expressed in our *P.*
129 *pastoris* expression system as two species differing in length or disulfide cross-linking pattern.
130 Mass spectrometry analysis of peptides purified from both HPLC peaks revealed identical
131 molecular weights (Supplementary Figure S1) as expected for NCR13 with three disulfide bonds,
132 narrowing our suspicion to different disulfide bonding patterns. Across various batches of purified
133 NCR13, peak 1 was consistently observed to contain less peptide than peak 2 (Supplementary
134 Table S1). Peak 1 and peak 2 peptides are hereafter referred to as NCR13_peptide folding variant
135 1 (NCR13_PFV1) and NCR13_PFV2 respectively.

136 To further characterize both NCR13_PFVs, we performed NMR structural analysis of $^{15}$N-
137 labeled NCR13_PFV1 and NCR13_PFV2. Figure 2A and B show the assigned $^{1}$H-$^{15}$N HSQC
138 spectra for NCR13_PFV1 and NCR13_PFV2, respectively. The broad dispersion of amide
139 chemical shifts in both spectral dimensions is a standard feature of a structured peptide (Yee et al.,
140 2002). As illustrated in Figure 2, assignment of both spectra was consistent with the primary amino
141 acid sequence of NCR13. However, the pattern of the fingerprint $^{1}$H-$^{15}$N HSQC spectrum for both
142 peptides was clearly different, suggesting their structures were unique. Given that the primary

143 amino acid sequence of NCR13 contains six cysteine residues (C4, C10, C15, C23, C28, and C30)
144 that can form fifteen different patterns of intramolecular disulfide bonds when all six are oxidized,
145 our attention immediately focused on a different disulfide bond pattern for the two peptides.
146 Treatment of both peptides with the reducing agents dithiothreitol (DTT) or tris(2-carboxyethyl)
147 phosphine resulted in the identical $^{1}H$-$^{15}N$ HSQC spectrum shown in Figure 2C, illustrating that
148 the parent primary amino sequence was identical for both peptides. Note that when the NCR13
149 cysteines are all in the reduced (dithiol) state, dispersion of amide chemical shifts in both spectral
150 dimensions were distinctively narrow, a standard feature of an unstructured protein (Shaw et al.,
151 2020; Yee et al., 2002). As observed for *M. truncatula* NCR044 (Velivelli et al., 2020), disulfide
152 bond formation is essential to stabilize the elements of secondary structure observed in the
153 oxidized state because in the reduced state the peptide is largely disordered.

154 Disulfide bond formation between all six cysteine residues in NCR13_PFV1 and
155 NCR13_PFV2 was unambiguously verified from the NMR chemical shifts of the cysteine side
156 chain β-carbon. In general, the cysteine $^{13}C^{\beta}$ chemical shift is greater than 35 ppm in the oxidized
157 state and under 32 ppm in the reduced state. As summarized in Supplementary Table S2, the $^{13}C^{\beta}$
158 chemical shift for all six cysteines in both isoforms of oxidized NCR13 are between 37 and 48
159 ppm, indicating they are all oxidized in NCR13_PFV1 and NCR13_PFV2. Due to the number of
160 potential disulfide bond patterns that the six cysteine residues can adopt, it was not possible to use
161 NMR structures in early calculations to unambiguously deduce disulfide bond pairs from $^{1}H$-$^{1}H$
162 NOEs that arise due to proximal γ-sulphur atoms in the disulfide state. Instead, as previously
163 applied to NCR044, the disulfide bond pattern was inferred from the analysis of mass spectral data
164 for trypsin-digested, unlabeled protein in the oxidized and reduced states (Velivelli et al., 2020).
165 For NCR13_PFV2, this approach showed that the disulfide bonds were C4-C10, C15-C30, and

166 C23-C28 (Supplementary Figure S2). For NCR13_PFV1, despite extensive modification of the
167 experimental procedures, this approach failed due to the hyperstability of this isoform towards
168 trypsinization. Consequently, the disulfide bond pattern predicted by AlphaFold (Jumper et al.,
169 2021) C4-C23, C10-C28, and C15-C30 was used to calculate the ensemble of NMR structures for
170 NCR13_PFV1. The two NCR13 isoforms share one identical disulfide bond, C15-C30, and
171 Supplementary Table S2 shows that these cysteine $^{13}C^{\beta}$ chemical shifts differ less than 0.5 ppm,
172 strongly suggesting this disulfide bond is present in both isoforms. As will be discussed below, this
173 disulfide bond pattern best supports the experimental NOE data.
174

175 **Three-dimensional NMR solution structures of NCR13_PFV1 and NCR13_PFV2**

176 To obtain structural insights into NCR13_PFVs, we performed NMR analyses of the oxidized
177 forms of these two peptides. Figure 3 illustrates a superposition of cartoon representations of the
178 final ensemble of structures calculated for the two NCR13 PFVs (left) with the main chain of a
179 single structure shown to the right of the ensemble with the disulfide bonds highlighted in different
180 colors. The elements of secondary structure are essentially identical in both isoforms, one anti-
181 parallel β-sheet (V20-I24, F27-V31) and a short a-helix (Q5 or S6–C10). However, the disulfide
182 bond pattern markedly alters the relative orientation of these elements of secondary structure. Both
183 peptides contain one identical disulfide bond, C15-C30, that ties the N-terminal end of the peptide
184 to approximately the middle of the linker region between the two elements of secondary structure.
185 The consequence is that in NCR13_PFV1 the α-helix sits over the top of the face of the β-sheet
186 while in NCR13_PFV2 the α-helix sits on the side of the β-sheet. This difference is better
187 illustrated in Supplementary Figure S3, a cartoon illustration of two representative structures
188 superimposed on the β-strand. This results in a smaller accessible surface area for NCR13_PFV1

189 (3188 ± 63 Å$^2$) than for NCR13_PFV2 (3357 ± 129 Å$^2$). The more compact structure for
190 NCR13_PFV1, with the disulfide bonds formed between C4, C10, C23, and C28 directed into the
191 interior of the peptide, may protect these disulfide bonds from reduction and contribute to the
192 hyperstability of NCR13_PFV1 towards reduction. Disulfide bonds may also be protected from
193 reduction because this NCR13 isomer is less dynamic. This suggestion is indirectly made by
194 comparing the ensemble of calculated solution structures illustrated in Figure 3. The ensemble of
195 structures calculated for NCR13_PFV1 converge to a greater extent than for NCR13_PFV2 with
196 the backbone (N-C$^a$-C=O) RMSD to the mean for the ordered residues almost twice as large for
197 NCR13_PFV2 (0.41 ± 13 Å versus 0.76 ± 20 Å, respectively; Supplementary Table S3). While
198 this difference reflects the greater number of NOEs observed for NCR13_PFV1 (316) than for
199 NCR13_PFV2 (119) (Supplementary Table S3) due to a more compact structure, it also indirectly
200 suggests the NCR13_PFV1 explores less conformational space than NCR13_PFV2.

201 To further verify that the AlphaFold predicted disulfide bond pattern was correct for
202 NCR13_PFV1, an NMR structure was calculated using only the NOE and TALOS+ (dihedral
203 angle) data (no hydrogen bonds) with the other possible disulfide bond pattern (C4-C28, C10-C23,
204 and C15-C30). In Supplementary Figure S4A, two representative cartoon structures that result
205 from the two possible disulfide bond patterns are superimposed on the β-strands. In the reversed,
206 C4-C28/C10-C23 disulfide pattern (yellow), the direction of α1 is also reversed relative to the β-
207 strand and this prevents the N-terminal region (T1-P3) from making close contact with the β-
208 strand. While most of the NOEs were satisfied in both structure calculations, long range
209 experimental NOEs between the N-terminal region of NCR13_PFV1 (T1-P3) and the β-strand
210 were only satisfied with the C4-C23/C10-C28 disulfide pattern used in the structure deposited to
211 the PDB (8UTM), suggesting this pattern was correct. Furthermore, as shown in Supplementary

212 Figure S4B, the predicted AlphaFold structure for NCR13_PFV1 was like the experimental
213 structure (8UTM). In both structures, the β-sheet is almost identical with the major difference a
214 slightly shorter α-helix displaced two residues (D7-K11 versus Q5-C10 experimentally) that packs
215 against the β-strand a bit differently in the AlphaFold structure (green). Most relatively, the N-
216 terminal region (T1-P3) folds towards the β-strand in the AlphaFold predicted structure, as verified
217 experimentally with the long-range NOEs between these regions.
218

219 **NCR13_PFV1 exhibits much greater antifungal activity against fungal pathogens than**
220 **NCR13_PFV2**

221 Having found striking differences in their NMR structures, we investigated the *in vitro*
222 antifungal activity of NCR13_PFV1 and NCR13_PFV2 against three necrotrophic plant fungal
223 pathogens (Velivelli et al., 2020). NCR13_PFV1 inhibited the growth of *B. cinerea* at the Minimal
224 Inhibitory Concentration (MIC) of 0.09 μM. Conversely, NCR13_PFV2 inhibited *B. cinerea* at the
225 MIC of 1.5 μM (Figure 4A-C), seventeen-fold higher than that of NCR13_PFV1. Chemically
226 synthesized NCR13 had a MIC of 3 μM, two-fold higher than NCR13_PFV2 (Figure 4B),
227 suggesting that this fully reduced synthesized product was yet another isoform of NCR13 and
228 illustrating the importance of disulfide bonds for antifungal activity. Similarly, NCR13_PFV1
229 showed several fold greater antifungal activity against *Fusarium virguliforme,* and *Sclerotinia*
230 *sclerotiorum* compared to NCR13_PFV2 (Figure 4A). Overall, these results reveal that
231 NCR13_PFV1 is a much more potent antifungal peptide compared to NCR13_PFV2.
232

233 **Disulfide bonds in NCR13_PFV1 contribute to the antifungal activity and formation of**
234 **peptide folding variants**

235 Fully oxidized NCR13_PFV1 contains three disulfide bonds: C4-C23, C10-C28, and C15-
236 C30. The potent antifungal activity of NCR13_PFV1 against *B. cinerea* at nanomolar
237 concentrations prompted us to investigate the contribution of each disulfide bond towards
238 antifungal activity and the formation of folded variants when expressed in *P. pastoris*. We carried
239 out functional analysis of these disulfide bonds by creating three dual Cys to Ser variants to
240 systematically remove one disulfide bond: NCR13_C4S-C23S, NCR13_C10S-C28S, and
241 NCR13_C15S-C30S variants (Figure 5A). These knockout variants were expressed in *P. pastoris*
242 and purified. HPLC profiles of NCR13_C4S-C23S, and NCR13_C15S-C30S revealed a single
243 peak whereas NCR13_C10S-C28S revealed two peaks (Figure 5B), the latter observation
244 suggesting NCR13_C10S-C28S folded with at least two different disulfide bonding patterns. Mass
245 spectrometry analysis confirmed the expected molecular mass of each peptide (Supplementary
246 Table S4), consistent with them being in an oxidized state. Therefore, our results indicate that the
247 disulfide pairing of C4-C23 and C15-C30 is essential for the formation of NCR13_PFVs.
248 All three single disulfide bond knockouts had lower antifungal activity against *B. cinerea*
249 compared to NCR13_PFV1, as summarized in Figure 5. NCR13_C4S-C23S and NCR13_C15S-
250 C30S both inhibited *B. cinerea* with a MIC value of 1.5 and 0.75 μM respectively, while the
251 products in the two NCR13_C10S-C28S HPLC peaks had a MIC of 3 μM (Figure 5C and D).
252 While we were unable to confirm the disulfide bonding pattern in each of these knockout variants,
253 the MIC data indicates that each disulfide bond contributes to the antifungal activity of
254 NCR13_PFV1 (Figure 5C and D). Indeed, a NCR13 construct with all six Cys residues replaced
255 with Ser (NSR13) was inactive against *B. cinerea* even at the highest tested concentration, 24 μM
256 (Figure 5C and D; Supplementary Figure S4). It is likely that NSR13 is unfolded, as suggested by
257 the NMR data for reduced NCR13 (Figure 2) and its late elution time on a reverse phase column.

258 Therefore, it can be concluded that each disulfide bond contributes to the antifungal activity of the
259 NCR13.
260
261 **Identification of the sequence motif governing the antifungal activity of NCR13**
262 To identify the sequence motif governing the antifungal activity of NCR13 against *B.*
263 *cinerea*, we purchased chemically synthesized alanine scanning variants NCR13_AlaV1 through
264 NCR13_Ala5 (Figure 6A). These variants contained a string of three to five consecutive Ala
265 residues substituted throughout the NCR13 sequence. We then compared their antifungal activity
266 relative to a chemically synthesized NCR13. Notably, our findings revealed that NCR13_AlaV2,
267 NCR13_AlaV3, and NCR13_AlaV4 had no antifungal activity against *B. cinerea* at the highest
268 tested concentration, 12 μM (Figure 6A, Supplementary Figure S6A), whereas NCR13 inhibited
269 this pathogen at an MIC of 3 μM. This data suggested that a 13-residue, Lys-rich motif,
270 KKFA**C**RKPKVPK**C,** located in the random coil and β-strand region, was a major determinant of
271 NCR13 antifungal activity. We further explored the importance of this motif by testing antifungal
272 activity of NCR13_AlaV3 expressed in *P. pastoris* to allow formation of disulfide bonds and found
273 that it also lacked antifungal activity against *B. cinerea* like the chemically synthesized
274 NCR13_AlaV3 (Supplementary Figure S6B). It is noteworthy that NCR13_AlaV1 and
275 NCR13_AlaV5 also displayed 2- and 4-fold reduction, respectively, in the antifungal activity
276 against *B. cinerea* indicating that the N-terminal QSDKD and C-terminal INGF motifs are
277 relatively minor contributors to the antifungal activity of this peptide. (Figure 6A).
278
279 **NCR13_PFV1 disrupts the plasma membrane of *B. cinerea* faster than NCR13_PFV2**

280 Since NCR13_PFV1 exhibits ~17-fold more potent antifungal activity against *B. cinerea*
281 than NCR13_PFV2, we hypothesized that the difference in antifungal activity lies in differential
282 membrane permeabilization ability. To test this hypothesis, we performed SYTOX$^{TM}$ Green (SG)
283 assays to examine the ability of NCR13_PFV1 and NCR13_PFV2 at 0.09 μM to permeabilize the
284 plasma membrane of *B. cinerea* germlings. SG, a membrane-impermeant dye, binds to nucleic
285 acids and is an indicator of membrane permeability. Average fluorescence intensities were
286 measured along different time points and NCR13_PFV1 showed much higher fluorescence
287 intensity within exposed cells than NCR13_PFV2 (Figure 7A and B). After 10 min, SG uptake
288 was observed in germlings challenged with NCR13_PFV1 but not in germlings challenged with
289 NCR13_PFV2. After 20 min, a very strong SG uptake signal was observed in NCR13_PFV1
290 treated germlings, but only a modest signal in NCR13_PFV2 treated germlings (Figure 7A and B).
291 Thus, NCR13_PFV1 inhibited fungal growth to a greater degree than NCR13_PFV2 at nanomolar
292 concentration in part by permeabilizing the plasma membrane of *B. cinerea*.
293
294 **NCR13_PFV1 and NCR13_PFV2 reveal quantitative differences in their binding to multiple**
295 **membrane phospholipids**
296 Antifungal plant defensins gain entry into fungal cells and bind to a variety of bioactive
297 phospholipids resident on the plasma membrane (Parisi et al., 2019). We speculated that
298 NCR13_PFV1 and NCR13_PFV2 differ in their phospholipid binding specificity in the context
299 of membrane bilayer. Therefore, we used phospholipid strip assays to determine if NCR13_PFVs
300 bind to different phospholipids. Our findings revealed that both NCR13_PFV1 and NCR13_PFV2
301 interacted with several phospholipids, including phosphatidylinositol 4-phosphate [PI(4)P] and
302 PI(4,5)$P_2$ (Figure 7C). NCR13_PFV2 displayed significantly stronger binding affinity to

303 phosphoinositides such as PI(3)P, PI(4)P, PI(5)P, PI(4,5)$P_2$, and PI(3,4,5)$P_3$ than NCR13_PFV1
304 (Figure 7D). The interaction of PI(4)P and PI(4,5)$P_2$ with NCR13_PFV1 and NCR13_PFV2 were
305 further validated using a polyPIPosome binding assay (Figure 7E). Nevertheless, the significance
306 of the phospholipid binding differences between the two peptides for their antifungal activity
307 requires further investigation. Since several antifungal plant defensins bind to membrane
308 phospholipids to oligomerize and induce membrane permeabilization (Poon et al., 2014), we tested
309 the ability of NCR13_PFV1 and NCR13_PFV2 to oligomerize by incubating the peptides with the
310 biochemical cross-linker bis(sulfosuccinimidyl)suberate ($BS_3$) in the presence and absence of
311 PI(4,5)$P_2$. NCR13_PFV1 formed oligomers both in the presence and absence of PI(4,5)P2. On the
312 other hand, NCR13_PFV2 formed higher order oligomers, but, only at higher concentrations (115
313 μM and 330 μM) of PI(4,5)$P_2$ (Supplementary Figure S7). Therefore, further investigation is
314 required to determine whether phospholipid binding, including PI(4,5)P2, and the oligomerization
315 of NCR13_PFVs are critical for fungal cell killing.
316
317 **NCR13 PFV1 is internalized faster in germling cells of *B. cinerea* than NCR13_PFV2**
318 Due to its much greater antifungal activity *in vitro* against *B. cinerea*, we hypothesized that
319 NCR13_PFV1 exhibited faster entry into fungal cells at its MIC than NCR13_PFV2. To test this
320 hypothesis, we exposed *B. cinerea* germlings to 0.09 μM DyLight550-labeled NCR13_PFV1 and
321 NCR13_PFV2 and monitored their entry into germlings of *B. cinerea* using confocal microscopy.
322 Within ~30 min, NCR13_PFV1 penetrated the germlings; however, NCR13_PFV2 did not enter
323 the germlings (Figure 8A and B). At a concentration of 1.5 μM, NCR13_PFV1 started entering
324 germlings in ~4 min, while NCR13_PFV2, after briefly gathering on the cell surface (Figure 8C,

325 white arrowheads), started entering germlings at ~8 min. Unlike NCR13_PFV2's lack of entry at
326 0.09 µM, delayed entry of NCR13_PFV2 was evident at 1.5 µM (Figure 8C and D).
327 Following entry into *B. cinerea* germling cells, both NCR13_PFV1 and NCR13_PFV2
328 accumulated in distinct subcellular foci (Figure 8E, white arrows). Further localization studies
329 using the nuclear staining dye Hoechst 33258 revealed that both peptides were localized in the
330 nuclei. To determine if each peptide was sub-localized within the nucleolus, we used the nucleolus-
331 specific RNA staining dye Nucleolus Bright Green. As shown in Figure 8F, each peptide was
332 localized within the nucleolus of germling cells suggesting that each peptide likely binds to
333 ribosomal RNA (rRNA) or proteins and interferes with protein synthesis.
334 To gain further insight into the MoA of NCR13_PFV1 and NCR13_PFV2, we assessed the
335 stability of each peptide once inside *B. cinerea* cells. We challenged *B. cinerea* germlings with
336 each peptide separately for two different time points, 2 h and 4 h, and tested the stability of each
337 peptide in fungal cells through western blot analysis. An NCR13 polyclonal antibody capable of
338 binding to each peptide with equal affinity was used for this analysis (Supplementary Figure S8).
339 NCR13_PFV1 accumulated in germling cells within 2 h and accumulates further after 4 h. In
340 contrast, much less NCR13_PFV2 accumulated in germling cells within 2 h and was strongly
341 decreased by 4 h (Supplementary Figure 8E). Therefore, we highlight NCR13_PFV1 more rapidly
342 enters fungal cells than NCR13_PFV2, and once inside NCR13_PFV1 is more stable than
343 NCR13_PFV2.
344
345 **NCR13_PFV1 binds to rRNA and is a more potent inhibitor of protein translation *in vitro***
346 **than NCR13_PFV2**

347 Since NCR13_PFVs are localized in the nucleoli of *B. cinerea*, we decided to test the
348 binding of each peptide to rRNA. This was accomplished with an Electrophoretic Mobility Shift
349 Assay (EMSA) (Hellman & Fried, 2007) by incubating each peptide with total rRNA isolated from
350 *B. cinerea* germlings. Our results showed that NCR13_PFV1 retarded the mobility of the rRNA at
351 all concentrations greater than 0.18 μM, while NCR13_PFV2 showed no binding to rRNA until 3
352 μM (Figure 9A; Supplementary Figure S8). Therefore, it is evident that NCR13_PFV1 exhibits
353 stronger binding affinity to rRNA than NCR13_PFV2.
354 Next, we tested the ability of the NCR13_PFVs to inhibit protein translation *in vitro* because we
355 hypothesized that NCR13_PFV1 may be a more potent inhibitor of protein translation than
356 NCR13_PFV2. This was accomplished using a wheat germ *in vitro* translation system based on a
357 luciferase activity (Olliver et al., 1985). Protein translation inhibitory activity of each peptide was
358 concentration dependent (Figure 9B). NCR13_PFV1 inhibited translation more effectively than
359 NCR13_PFV2 at concentrations more than 0.75 μM. At 24 μM, NCR13_PFV1 almost completely
360 halted translation compared to the ~50% inhibition by NCR13_PFV2 (Figure 9B). Based on these
361 results, the difference in the antifungal potency of NCR13_PFVs may be partly due to the
362 inhibition of protein translation *in vivo* with NCR13_PFV1 being a more potent protein translation
363 inhibitor in *B. cinerea*.
364

365 **NCR13_PFV1 is more potent than NCR13_PFV2 semi-*in planta***

366 Next, we compared the semi-*in planta* antifungal activity of NCR13_PFV1 and
367 NCR13_PFV2 using detached leaves of pepper as previously described (Li et al., 2019). To
368 eliminate leaf-to-leaf variation, both peptides were added instantaneously with freshly prepared *B.*
369 *cinerea* spores to the same leaf, along with a no-peptide control, at different concentrations (3, 1.5,

370 and 0.09 μM) (Supplementary Figure S9A). Leaves were evaluated for reduction of gray mold
371 lesions through measurement of photosynthetic efficiency Fv/Fm (variable fluorescence over
372 saturation level of fluorescence) using CropReporter images. At 3 μM and 1.5 μM NCR13_PFVs,
373 no disease symptoms were visualized (Supplementary Figure S9B) and no significant difference
374 in photosynthetic efficiency (Supplementary Figure S9C) was observed, whereas the no-peptide
375 control contained visible lesions and reduced photosynthetic efficiency. At 0.09 μM, only
376 NCR13_PFV1 effectively suppressed the formation of visible lesions, while NCR13_PFV2
377 resulted in lesion sizes similar to the no-peptide control (Supplementary Figure S9B). Moreover,
378 a decrease in photosynthetic efficiency observed for NCR13_PFV1 was milder than observed for
379 NCR13_PFV2. Together, this data further illustrates that NCR13_PFV1 is a more potent antifungal
380 agent than NCR13_PFV2 in terms of preventing and reducing gray mold lesions on peppers
381 (Supplementary Figure S9B and C). These observations correlate well with the *in vitro* antifungal
382 activity of each peptide. Based on this comparative study of their antifungal activity using a
383 detached leaf assay, NCR13_PFV1 was judged to be a more promising peptide-based fungicide *in*
384 *planta* (see below).
385

386 **Spray-applied NCR13_PFV1 is more effective in reducing gray mold disease symptoms in**
387 **pepper and tomato plants than NCR13_PFV2**

388 To determine if the *in vitro* and semi-*in planta* antifungal activity of these peptides
389 translated to antifungal activity *in planta*, we tested the curative protection afforded by
390 NCR13_PFV1 and NCR13_PFV2 against *B. cinerea* by spray application on pepper plants. Four-
391 week-old pepper plants were pre-inoculated with freshly prepared *B. cinerea* spores. At 8 h post-
392 inoculation, peptide at 1.5 and 3 μM concentration was sprayed onto pepper leaves. At 72 h post-

393 inoculation. disease symptoms were evaluated by comparing photosynthetic efficiency (Fv/Fm) of
394 the pathogen-challenged peptide-sprayed plants with the no-peptide control. Green areas indicate
395 a high photosynthetic rate and healthy tissue, while yellow to red areas indicate reduced
396 photosynthetic rate and diseased tissue. As evidenced by their higher Fv/Fm values, leaves of
397 pepper plants sprayed with NCR13_PFV1 at 1.5 and 3 μM had greater reduction in gray mold
398 lesions than the leaves of pepper plants sprayed with NCR13_PFV2 at the same concentrations
399 (Figure 10A and B). Pepper plants sprayed with 1.5 μM NCR13_PFV2 showed no significant
400 control ($p>0.05$) of gray mold when compared to the no-peptide control plants suggesting
401 NCR13_PFV2 is unable to reduce gray mold disease symptoms at lower concentration (Figure
402 10A-C). Correspondingly, the data aligns with the observation that NCR13_PFV1 markedly
403 decreased the percentage of disease severity relative to NCR13_PFV2 at both treatment
404 concentrations (Figure 10C). However, NCR13_PFV2 sprayed at 3 μM was able to provide
405 significant curative protection compared to control plants (Figure 10A-C), but it was not as
406 effective as NCR13_PFV1. A similar observation was made when four-week-old tomato plants
407 were also pre-inoculated with *B. cinerea* spores followed by spraying 3 μM of each peptide
408 (Supplementary Figure S10A-C). The NCR13_PFVs significantly decreased the disease severity,
409 with NCR13_PFV1 demonstrating the most pronounced effect (Figure S10B). NCR13_PFV1 and
410 NCR13_PFV2 inhibited gray mold disease 90% and 40%, respectively (Supplementary Figure
411 S10C). In summary, these data indicate higher potential of NCR13_PFV1 for management of the
412 gray mold disease in pepper and tomato plants.
413

414 **Discussion**

415 NCR13 is a highly cationic peptide among the 63 predicted NCR peptides expressed in chickpea
416 nodules (Montiel et al., 2017). In this study, we discovered that NCR13 expressed in *P. pastoris*
417 forms two isomers, NCR13_PFV1 and NCR13_PFV2, which have identical amino acid sequence
418 and molecular mass but differ in their disulfide pairing patterns. We report a comparative analysis
419 of the structure, *in vitro* and semi-*in planta* antifungal activity and MoA of NCR13_PFVs. Our
420 results support the proposal that disulfide cross-linking provides an additional source of structural
421 and functional diversity in NCR peptides (Shabab et al., 2016).

422 Four- or six-cysteine NCRs are highly diverse in their primary sequences and are predicted to
423 be structurally different. Previously, two solution NMR structures of NCR044 and NCR169, each
424 containing two disulfide bonds, were solved (Isozumi et al., 2021; Velivelli et al., 2020). The
425 NCR044 structure was largely disordered, dynamic and contained a single α-helix and a β-sheet
426 (Velivelli et al., 2020). Structural analysis revealed that the two NCR169 isomers contained only
427 one short, two-stranded β-sheet, with one isomer being more extended and flexible while the other
428 was more compact and constrained (Isozumi et al., 2021). To date, a three-dimensional structure
429 for a six-cysteine NCR peptide has not been reported. Here, we report the first solution structures
430 of two NCR13 disulfide isomers each containing an α-helix and β-sheet. Nevertheless, unique
431 pairing of two out of the three disulfide bonds significantly alters how these secondary structure
432 elements fold upon each other rendering NCR13_PFV1 more compact and resistant to digestion
433 by trypsin or reduction by dithiothreitol. It is striking that *P. pastoris* generates two disulfide
434 variants that are structurally different and raises the question of whether these variants are also
435 expressed in the differentiating nodules of chickpea to perform different biological activities. In
436 an earlier study, three disulfide variants of NCR247 containing four cysteines were generated using
437 chemical synthesis and *in vitro* folding. NCR247 variants were found to have distinct patterns of

438 biological activities such as bacterial gene expression, inhibition of bacterial cell division, protein
439 translation and antibacterial activity (Haag et al., 2012; Shabab et al., 2016). These observations
440 suggest that NCR peptides can form disulfide variants *in vitro* or in an appropriate expression host,
441 leading to diverse biological activity. Whether disulfide variants of NCR13, NCR247, or NCR169
442 are formed *in vivo* in nodules to control symbiosis in IRLC legumes remains an open question. In
443 contrast to NCR peptides, plant defensins with eight cysteines expressed in *P. pastoris* are only
444 observed as one species with an invariant disulfide pairing pattern (Kovaleva et al., 2020).

445 To our knowledge, this study is the first detailed investigation of a chickpea NCR peptide and
446 its antifungal action. Our data demonstrates that disulfide folding variants of NCR13 produced in
447 *P. pastoris* exhibit profound differences in antifungal activity against multiple fungal pathogens of
448 economic importance. NCR13_PFV1 possesses highly potent antifungal activity against *B. cinerea*
449 and other pathogens, showing a four- to sixteen-fold greater activity compared to NCR13_PFV2.
450 Remarkably, we found that the antifungal activity of NCR13_PFV1 is greater than other NCR
451 peptides reported to date in literature (Lima et al., 2020). It is noteworthy that enhanced antifungal
452 activity of both NCR13_PFVs produced in *P. pastoris* compared to chemically synthesized NCR13
453 without disulfide bond, underscores the critical role of disulfide bonds for antifungal activity.
454 Furthermore, the formation of all three disulfide bonds is essential for highly potent antifungal
455 activity of NCR13_PFV1 as removal of each disulfide bond resulted in a significant loss of its
456 antifungal activity against *B. cinerea*. In addition, Cys residues are essential for the antifungal
457 activity of NCR13 as their replacement with Ser leads to complete loss of antifungal activity.
458 Acting as molecular anchors, disulfide bonds provide stability to the three-dimensional structure
459 of proteins and peptides. They set the constraints for distance and angles between connected
460 cysteine residues, thus favoring the stability of the protein's folded state over its unfolded form

461 (Wedemeyer et al., 2000). Furthermore, the insertion of cysteine residues into *de novo* designed
462 peptides has produced hyper-stable peptides with unique tertiary structures that form the basis for
463 new peptide-based drugs (Bhardwaj et al., 2016; Buchko, Pulavarti, et al., 2018). The impact on
464 antifungal activity of knocking out two instead of just one disulfide bond is yet to be investigated.
465 Further, evaluating the three-dimensional structures of these double disulfide bond knockout
466 variants will provide deeper insight into structure-activity relationships of this unique NCR
467 peptide. *P. pastoris* has been the eukaryotic organism of choice for producing cysteine-rich
468 peptides to ensure formation of the correct disulfide bond patterns (Karbalaei et al., 2020). It is
469 intriguing that NCR13 expression results in the formation of two disulfide folding variants in *P.*
470 *pastoris*. In this context, it is critical to observe that knocking out either the C4-C23 or C15-C30
471 disulfide bond in NCR13_PFV1 results in the formation of one peak on HPLC, whereas knocking
472 out the C10-C28 bond still results in the formation of two distinct peaks. Mass spectrometry
473 analysis shows that peptides from two HPLC peaks of the C10-C28 knockout and one HPLC peak
474 in the C4-C23 and C15-C30 knockouts are in the oxidized state. Therefore, it is likely they are in
475 a folded/oxidized form. Finally, understanding the molecular mechanisms governing the
476 generation of disulfide variants of specific antifungal NCR peptides could pave the way for
477 production of targeted disulfide structural variants in *P. pastoris* with enhanced antifungal activity.
478 Antifungal peptides with potent fungicidal activity and multiple MoA are attractive candidates
479 for development as spray-on fungicides. NCR13 has a promise as one such candidate. For instance,
480 ability to permeabilize the plasma membrane of fungal pathogens is a common MoA of plant
481 cysteine-rich antifungal peptides including NCRs (Ordogh et al., 2014). NCR13_PFV1 can
482 permeabilize the plasma membrane of *B. cinerea* rapidly at very low concentrations. The
483 membrane disrupting ability of NCR13_PFV1 is far greater than that of NCR13_PFV2 and

484 NCR044 (Velivelli et al., 2020). Both NCR_PFVs bind to the same phospholipids on lipid strips
485 with different binding intensity. However, it is not clear what role, if any, phospholipid binding
486 plays in conferring increased membrane disrupting ability of NCR13_PFV1 and this aspect
487 remains to be elucidated. In addition, NCR13_PFV1 gains rapid entry into the interior of fungal
488 cells compared to NCR13_PFV2. It is plausible that more compact folding of NCR13_PFV1
489 allows it to more quickly penetrate the cell wall and pass through the outer and inner leaflets of
490 the plasma membrane. This is supported by the fact that *B. cinerea* germlings challenged with 1.5
491 μM of each peptide showed NCR13_PFV1 enters fungal cells in much greater levels after 2 h than
492 NCR13_PFV2. Moreover, once inside the cells, NCR13_PFV1 accumulates stably for at least 4 h
493 whereas NCR13_PFV2 tends to degrade in this time. Greater stability of NCR13_PFV1 to
494 proteolysis might be a major contributing factor to its much greater antifungal activity against this
495 pathogen, an observation that warrants further investigation.

496 Subcellular localization studies showed that NCR_PFVs are targeted to nucleoli in the
497 germlings of *B. cinerea* suggesting that these peptides are targeting ribosomal biogenesis or protein
498 translation machinery as part of their MoA as proposed earlier for the MoA of NCR044 (Velivelli
499 et al., 2020). In support of this hypothesis, we found that addition of each NCR13_PFVs to the *in*
500 *vitro* translation system inhibited protein synthesis in a concentration dependent manner.
501 NCR13_PFV1 proved to be more effective in inhibiting protein translation *in vitro*. NCR13_PFV1
502 also binds to *B. cinerea* rRNA at a lower concentration (0.37 μM) than NCR13_PFV2 (6 μM).
503 Further research is needed to determine if differences in rRNA binding affinity and protein
504 translation inhibition *in vitro* translate to profound differences in their antifungal activity *in vivo*.
505 NCR peptides appear to target protein translation as part of their antimicrobial mechanism as
506 evidenced by *M. truncatula* NCR247 inhibiting protein translation *in vitro* by binding to ribosomal

507 proteins (Farkas et al., 2014; Shabab et al., 2016). Plant defensin MtDef4 also inhibits protein
508 translation *in vitro* by binding to ribosomal proteins, but not to ribosomal RNA (Li et al., 2024).
509 Besides that, it is likely that NCR13_PFV1 and NCR13_PFV2 have different, yet unidentified,
510 intracellular targets which will be the subject of future investigation.

511 Fungicides currently used commercially for management of fungal diseases target ergosterol
512 biosynthesis, succinate dehydrogenase and cytochrome $bc_1$ complex. These targets are prone to
513 rapid development of fungal resistance (Hawkins & Fraaije, 2018). Small NCR peptides with
514 multi-faceted MoA have emerged as potential candidates for development as bioinspired
515 fungicides. We have previously demonstrated efficacy of NCR044 as a spray-on fungicide for
516 management of gray mold in tomato (Velivelli et al., 2020). Here, we report NCR13 is also a multi-
517 target antifungal peptide that reduces gray mold disease symptoms curatively when sprayed on
518 pepper and tomato plants. Consistent with its *in vitro* and semi-in planta antifungal activity,
519 NCR13_PFV1 affords greater protection against gray mold disease than NCR13_PFV2 in both
520 pepper and tomato plants. NCR13 is amenable to large scale recombinant production in a bio-
521 fermenter using *P. pastoris* expression system. However, further characterization of NCR13 is
522 needed, including demonstrating its efficacy for control of gray mold and other diseases in large-
523 scale greenhouse and field tests, assessment of off-target activity against mammalian cells and
524 phytotoxicity. In summary, this study demonstrated that disulfide bond pairing pattern has a
525 profound impact on the *in vitro* antifungal activity, MoA, and *in planta* antifungal activity of
526 chickpea NCR13. As illustrated in Figure 11, the graphical abstract illustrates the key findings of
527 our study. Overall, our work underscores the significance of disulfide cross-linking in enhancing
528 the efficacy of antifungal peptides for agricultural use.

529

530 **Materials and Methods**

531 **Fungal Cultures and Spore Suspension**

532 *B. cinerea* strain T4 was cultured in V8 medium for 3 weeks at 25°C. Fungal spores were collected
533 by flooding the fungal growth plates with water and scraped using sterile spreader. The spore
534 suspension was filtered through two layers of Miracloth, followed by centrifugation at 12,000 g
535 for 2 minutes (min) and subsequently washed twice with sterile water. Lastly, fungal spores were
536 resuspended in Synthetic Fungal Media (SFM) (Liang et al., 2001). The spore suspension was
537 adjusted to the desired spore density of about $10^5$ spores/mL using a hemocytometer. *Fusarium*
538 *virguliforme (F. virguliforme*) was grown and maintained regularly in potato dextrose agar (PDA)
539 (Difco Laboratories) medium. Two weeks old *F. virguliforme* plates were used to collect spores as
540 described above for *B. cinerea* followed by centrifugation and washing step. Spores were counted
541 using a hemocytometer and adjusted to the final concentration of $10^5$ spores/mL in 2X SFM media.
542 *Sclerotinia sclerotiorum* obtained from the field of pennycress in Illinois was grown on PDA
543 medium at room temperature.

544 **Expression and purification of NCR13**

545 For expression in *P. pastoris*, the published amino acid sequence of the mature NCR13 peptide
546 (Montiel et al., 2016) was used for synthesis of the codon-optimized gene (GenScript). The NCR13
547 gene was expressed in *P. pastoris* X33 using either a SacI linearized pPICZα-A integration vector
548 (Invitrogen) or at XhoI and XbaI restriction sites. NCR13 was purified using a CM Sephadex C-
549 25 cation-exchange chromatography as described (Velivelli et al., 2020). After induction, cell-free
550 supernatant was collected after centrifugation (10,000×g) at 4 °C for 20 min, and the pH was
551 adjusted to 6.0. The supernatant was passed through cation-exchange resin, CM Sephadex C-25
552 (Sigma-Aldrich, Cat No: C25120) previously equilibrated with binding buffer (25 mM Sodium

553 Acetate Anhydrous, pH 6.0) using an AKTA FPLC. Peptides bound to the resin were eluted using
554 the elution buffer (1M NaCl, 50 mM Tris, pH 7.6). The FPLC fraction containing NCR13 was
555 concentrated and desalted using an Amicon Stirred Cell with a 3-kD cutoff membrane (Millipore,
556 Cat No: PLBC04310) and further purified by reverse phase C18-HPLC. HPLC fractions collected
557 separately for NCR13_PFV1 and NCR13_PFV2 were lyophilized and re-suspended in nuclease-
558 free water. Peptide concentrations were determined using the Pierce™ BCA Protein Assay Kit
559 (Thermo Scientific). NCR13 and alanine variants of NCR13 were chemically synthesized
560 (Biomatik) and further purified by in-house HPLC.

561 **Molecular weight determination**

562 Purified peptides were analyzed by LC-MS for accurate mass determination. Firstly, peptide
563 samples were cleaned using Thermo Scientific HyperSep C18 microscale SPE extraction tips and,
564 after dry-down, resuspended in 0.1% formic acid for LC-MS analysis. LC-MS was performed with
565 a Dionex RSLCnano HPLC coupled to an OrbiTrap Fusion Lumos (Thermo Scientific) mass
566 spectrometer using 80 min gradient (1-90% acetonitrile). Sample was resolved using a 75 µm x 15
567 cm PepMap C18 column (Thermo Scientific). MS spectra of protein ions of different charge-states
568 were acquired in positive ion mode with a resolution setting of 120,000 (at m/z 200). Mass
569 deconvolution was performed using ProteinProspector, Xcalibur (Thermo Scientific), and ESIprot
570 Online.

571 **Disulfide bond pattern identification for NCR13_PFV2 using mass spectrometry**

572 An aliquot of unlabelled, oxidzed NCR13_PFV2 was mixed with 20-fold less (in mass) trypsin,
573 incubated at room temperature for 1 h, and diluted in 50% acetonitrile, 0.1% formic acid to ~0.1
574 µM. The diluted samples were infused at 2 µL/min into a Thermo Q-Exactive Exploris 480
575 Orbitrap mass spectrometer with positive mode electrospray at 3.4 kV. The ion transfer tube was

576 at 320 °C, sheath gas at 2 psi, and auxiliary gas at 5 psi. Data-dependent acquisition was used
577 (MS1 resolution 60k, MS2 resolution 30k) over 8 min. Fragmentation spectra were collected with
578 higher-energy collisional dissociation (HCD) at 30% collision energy. Data were analyzed and
579 deconvoluted in FreeStyle (Thermo Scientific). Crosslinked peptides were identified using Byonic
580 (ProteinMetrics). Under the same conditions, NCR13_PFV1 could not be digested by trypsin (data
581 not shown).

582 **$^{15}$N isotopic labeling of NCR13 for NMR structural analysis**

583 The $^{15}$N-labeled NCR13_PFVs were prepared according to the protocol as described previously
584 (32) with minor modifications. NCR13-expressing *P. pastoris* X33 was grown at 28 ± 2˚C for two
585 days on a YPD plate containing 150 µg/mL Zeocin. A single colony was then inoculated into 5 mL
586 of YPD broth and grown overnight at 28 ± 2 ˚C on a rotary shaker at 225 ± 25 rpm. After overnight
587 growth, a 5 mL culture was transferred aseptically to 100 mL of FM23 medium (0.8% YNB
588 without amino acids and ammonium sulfate, 2 mg/L biotin, 1.2% $(NH_4)_2SO_4$, 0.3% $K_2HPO_4$,
589 0.28% $KH_2PO_4$, 2 ml/L PTM1 salts) containing 3% glucose. After 24 h, an additional 2% glucose
590 was added to the culture medium. After a growth phase of ~30 h and just prior to methanol
591 induction, the culture medium was adjusted to 0.02% $^{15}$N-ammonium chloride ($^{15}NH_4Cl$) and 0.1%
592 glucose. After 40 h, cells were harvested by centrifugation at 5,000 rpm at room temperature for
593 10 min, briefly washed with 0.2% glycerol, pelleted, and re-suspended in 100 mL FM23 medium
594 containing 1.2% $^{15}NH_4Cl$ and grown for 4-5 days at 25 ˚C at 225 ± 25 rpm. In the induction phase,
595 a low concentration of 0.2% methanol was initially added to the culture medium to induce protein
596 expression and gradually increased by 0.4% from 72 to 120 h (1.4% final). The labeled NCR13
597 peaks were purified from the *P. pastoris* growth medium following the same protocol used for the
598 unlabeled peptide.

**NMR spectroscopy of NCR13**

All NMR data were collected at 20˚C on $^{15}$N-labeled samples of oxidized NCR13_PFV1 and NCR13_PFV2 (~ 1 mM, 20 mM sodium acetate, 50 mM NaCl, pH 5.3) using Varian (Inova-600) or Bruker (Advent-750) spectrometers equipped with an HCN-probe and pulse field gradients. Except for the carbonyl resonances (which could not be assigned because making $^{13}$C-labeled samples in *P. pastoris* was too expensive), the $^{1}$H, $^{13}$C, and $^{15}$N chemical shifts of the backbone and side chain resonances were assigned from the analysis of two-dimensional $^{1}$H-$^{15}$N HSQC, $^{1}$H-$^{13}$C HSQC, $^{1}$H-$^{1}$H TOCSY, $^{1}$H-$^{1}$H NOESY, and $^{1}$H-$^{1}$H COSY spectra and three-dimensional $^{15}$N-edited NOESY-HSQC (mixing time = 90 ms) and $^{15}$N-edited TOCSY spectra. To obtain additional chemical shift assignments, inter- and intra-residue proton side chain restraints for proton near the residual water resonance, most of the two-dimensional data sets were also collected by lyophilizing and resuspending the sample in 99.8% $D_2O$. In preparing the latter sample, a $^{1}$H-$^{15}$N HSQC spectrum was collected ~10 min after the addition of $D_2O$ to identify slowly exchanging amides that could be used as hydrogen bond restraints in the structure calculations. To confirm oxidized NCR13_PFV1 and NCR13_PFV2 arose from different disulfide bond patterns of a common precursor primary amino acid sequence, both oxidized samples were reduced by making the NMR samples 5 mM in Dithiothreitol (DTT). While NCR13_PFV2 was reduced rapidly, it took more than 5 – 7 days to fully reduce NCR13_PFV1. All NMR data were processed using Felix 2007 (MSI, Molecular Simulations) software and analyzed with the program Poky (v3.115) (Lee et al., 2021). The assigned $^{1}$H, $^{13}$C, and $^{15}$N chemical shifts were referenced using indirect methods (DSS = 0 ppm) and deposited into the BioMagResBank database (www.bmrb.wisc.edu) under the accession numbers BMRB-31111 (oxidized NCR13_PFV1 8ULM) and BMRB-30979 (oxidized NCR13_PFV2 7TH8).

622 **NMR solution structure calculations for oxidized NCR13_PFV1 and NCR13_PFV2**

623 The protocols used to obtain solution structures for both peptides followed a similar approach
624 starting with the $^{1}$H, and $^{15}$N chemical shift assignments and peak-picked NOESY data serving as
625 initial experimental inputs in iterative structure calculations with the program CYANA (v 2.1)
626 (Guntert, 2004). The $^{1}$H, $^{13}$C, and $^{15}$N chemical shift assignments were also the primary basis for
627 the introduction of 24 (NCR13_PFV1) and 25 (NCR13_PFV2) dihedral Psi (ψ) and Phi (φ) angle
628 restraints identified with the program TALOS+ using the online webserver
629 (https://spin.niddk.nih.gov/bax/nmrserver/talos/) (Shen et al., 2009). Nine restraints between the
630 side chain sulfur atoms of C4-C23, C15-C30, and C10-C28 (NCR13_PFV1) and C4-C10, C15-
631 C30, and C23-C28 (NCR13_PFV1) (2.0-2.1 Å, 3.0-3.1 Å, and 3.0-3.1 Å for the Sγ-Sγ, Sγ-Cβ, and
632 Cβ-Sγ distances, respectively) (Buchko, Hewitt, et al., 2018; Velivelli et al., 2020) were introduced
633 on the basis of AlphaFold predictions for NCR13_PFV1 and high resolution mass spectrometry
634 analysis for NCR13_PFV2. Exhaustive attempts to identify the disulfide bond pattern for
635 NCR13_PFV1 using various mass spectrometric methods failed likely due to its hyperstability to
636 reduction by DTT or tris(2-carboxyethyl) phosphine. Backbone hydrogen bond restraints (1.8 –
637 2.0 Å and 2.7 – 3.0 Å for the NH–O and N-O distances, respectively) were added to the calculations
638 for proximate backbone amide-carbonyl groups present in early structure calculations that were
639 accompanied with slowly exchanging amides in the deuterium exchange experiment. The final
640 ensemble of 20 CYANA derived structures was then refined in explicit water with CNS (version
641 1.1) using the PARAM19 force field and force constants of 500, 500, and 1000 kcal for the NOE,
642 hydrogen bond, and dihedral restraints, respectively. For these water refinement calculations, 10
643 and 0 % were added to the upper boundary of the CYANA distance restraints for NCR13_PFV1
644 and NCR13_PFV2, respectively, and the lower boundary set to the van der Waals limit for both.

645 Structural quality was assessed using the online Protein Structure Validation Suite (PSVS, v1.5)
646 (Bhattacharya et al., 2007). Complete structural statistics are summarized in Supplementary Table
647 S3. The atomic coordinates for the final ensemble of 20 structures have been deposited in the
648 Research Collaboratory for Structural Bioinformatics (RSCB) under PDB codes 8ULM (NCR13_
649 PFV1) and 7TH8 (NCR13_ PFV2).

650 **Peptide uptake and stability assessment within *B. cinerea***

651 *B. cinerea* (~$10^5$ spores/mL) was inoculated in 10 mL of Potato Dextrose Broth (PDB) and
652 incubated in a shaker at 28ºC for 18 h. *B. cinerea* germlings were treated with 1.5 µM
653 NCR13_PFV1 and NCR13_PFV2 for 0, 2 and 4 h. Total proteins were extracted from the fungal
654 cells using 300 µL of HEPES buffer (100 mM HEPES, 5mM EDTA, 0.1% Triton-100, ProBlock™
655 Gold Yeast/Fungi Protease Inhibitor, pH 7.5) and centrifuged at 14000 rpm to remove cell debris.
656 The concentration of protein present in the supernatant was measured using Pierce™ BCA Protein
657 Assay Kit (Thermo Scientific). Total proteins (10 µg) were separated on a 4–20% SDS-PAGE gel
658 (Bio-Rad, TGX Stain-Free™ precast gels) and transferred to a nitrocellulose membrane. Equal
659 loading of proteins was checked using Ponceau S staining (Thermo Scientific). Immunoblotting
660 was performed using the custom synthesized anti-NCR13 polyclonal antibody (Biomatik) at a
661 concentration of 0.1 µg/mL followed by an incubation in the secondary anti-rabbit antibody
662 (Cytiva, Cat No: RPN4301) with a dilution of 1:20,000. ***In vitro* antifungal assay**

663 The antifungal activity of NCR13 against fungal pathogens was determined using the resazurin
664 cell viability assay as described previously (Chadha & Kale, 2015). Briefly, 45 µL of each peptide
665 dilution (0, 0.09, 0.1875, 0.375, 0.75, 1.5, 3 and 6 µM) was added to each well of the microtiter
666 plate containing 45 µL (~$10^5$ spores/mL) of spore suspension. Three biological replicates were
667 used for each treatment and the experiments were repeated three times. Resazurin at 0.1% (w/v)

668 was added to each well after incubation for 48 h. Images were taken at ~24 h. The Minimum
669 Inhibitory Concentration (MIC) for each peptide denotes the lowest concentration at which the
670 peptide halts the growth of fungus evident through a lack of color change from blue to colorless.
671 The *in vitro* antifungal activity of NCR13_PFVs against *S. sclerotiorum* was determined using a
672 24-well plate assay as described (Djami-Tchatchou et al., 2023). Mycelial plugs (1 mm in
673 diameter) cut from the growing edge of the two-day-old actively growing colony were transferred
674 from PDA media to a series of wells containing 250 µL of SFM.

675 **Internalization and permeabilization assays using confocal microscopy**

676 NCR13_PFV1 and PFV2 were labeled with DyLight550 amine reactive fluorescent dye following
677 the manufacturer's instructions (Thermo Scientific). *B. cinerea* germlings (50 µL, ~$5x10^4$
678 spores/mL) were treated with DyLight 550 labeled NCR13_PFV1 and NCR13_PFV2 (50 µL, 0.09
679 µM and 1.5 µM), and the fluorescence measured with excitation and emission wavelengths of 550
680 and 560-600 nm, respectively. Time-lapse confocal microscopy data with a z-stack at each time
681 point were acquired using a 63X water immersion objective lens (HC PL Apochromat CS2) at 30-
682 second intervals. For the membrane permeabilization assay, fluorescent dye SYTOX™ Green
683 (Thermo Scientific) at a concentration of 0.25 µM was used to determine the membrane
684 permeabilization of *B. cinerea* germlings as described previously (Li et al., 2019). Time lapse
685 imaging was performed to visualize the SYTOX™ Green entry upon treatment with 50 µL of 0.09
686 and 1.5 µM NCR13_PFVs. Imaging was performed on a Leica SP8 confocal microscope with
687 excitation at 488 nm and emission at 508–544 nm. Average fluorescence intensity measurements
688 were obtained using Fiji (Schindelin et al., 2012).

689 **Phospholipid binding assays**

Phospholipid binding of NCR13_PFVs were performed with PIP Strips (Echelon Biosciences) that are spotted with 100 pmol of various biologically active phospholipids. Peptide binding to the membrane strips was detected using monoclonal NCR13 antibody (0.1 µg/mL) followed by goat anti-rabbit IgG HRP (Cytiva RPN4301) at 1:20,000 dilution. The binding signals were detected using the SuperSignal West Pico Chemiluminescent Substrate Kit (Thermo Scientific) following the manufacturer's protocol. Quantitative analysis of the blot intensity was performed using Fiji (Schindelin et al., 2012).

**Oligomerization assay**

To determine the oligomerization status of the NCR13_PFVs, the peptides were prepared in PBS buffer at 1.5 mg/mL (5 µL/reaction) and incubated with specified concentrations of PI(4,5)P2. The cross-linking reaction was initiated by addition of 12.5 mM bis(sulfosuccinimidyl)suberate BS3 (Thermo Scientific) and then incubated for 30 min at room temperature. After incubation, tricine sample buffer was added to each sample and heat denatured at 95 ºC for 5 min. Samples were loaded on a 16.5% Tris-Tricine precast gel (Bio-Rad Laboratories). For SDS-PAGE, 5 µL of Precision Plus Dual Xtra Protein Standards (2–250 kDa) were used (Bio-Rad Laboratories). Oligomerization patterns were visualized using silver staining.

**PolyPIPosome binding assay**

The validation of the binding of NCR13_PFV1 and NCR13_PFV2 to phospholipids was further performed using a liposome binding assay. In this assay, polyPIPosome binding was conducted in 200 µL of binding buffer (20 mM HEPES pH 7.4, 120 mM NaCl, 1 mM EGTA, 1 mM $MgCl_2$, 1 mg/mL BSA, 0.2 mM $CaCl_2$, 5 mM KCl) plus 10 µL each of control PolyPIPosome, PI4P PolyPIPosomes, and $PIP_2$ PolyPIPosome (Echelon Biosciences). Subsequently, 2 µg of each peptide was added, and the mixture incubated for 1 h at room temperature. Following incubation,

liposomes were collected by centrifugation at 16,000 × g for 20 min, and the supernatant was collected. The pellet was subjected to three washes in 1 mL of binding buffer. After the washes, the pellet was resuspended in 40 µL of 2X Laemmli sample buffer. Both samples were reduced with 100 mM DTT and separated on a 4–20% TGX Stain-Free™ precast gels (Bio-Rad Laboratories). Proteins were then transferred to a nitrocellulose membrane and subjected to blotting using the NCR13 antibody.

**Electrophoretic mobility shift assay**

Total RNA was extracted and purified from *B. cinerea* grown in Potato Dextrose Broth (Fisher Scientific) using the NucleoSpin RNA Plus Mini kit (Takara Bio) according to manufacturer instructions. The gel shift experiments were performed by mixing 200 ng of the total RNA with different concentrations of NCR13 PFV1 and PFV2 (0-3 µM) in 20 µL of binding buffer (10 mM Tris-HCl, pH 8.0, 1 mM EDTA). The reaction mixtures were incubated for 1 h at room temperature and mixed with 4 µL of 6X gel loading dye (New England Biolabs). Following electrophoresis in 1.2% agarose gel containing SYBR safe DNA gel stain (Thermo Scientific) with TAE buffer at 120 V for 45 min, the gels were visualized using a Bio-Rad ChemiDoc XRS+ system.

***In vitro* translation assay**

*In vitro* translation was performed using the RiboMAX™ Large Scale RNA Production system and Wheat Germ Extract *in vitro* translation system (Promega). First, the luciferase DNA template (Promega) was transcribed to mRNA and translated to luciferase following the manufacturer's protocol. The luciferase enzyme activity was detected by the luciferase kit (Promega) using a luminometer (Tecan). Different concentrations of NCR13_PFV1 and NCR13_PFV2 were used to determine their translation inhibition ability. Sterile water was added to the *in vitro* translation system as a negative control and a fungal translation inhibitor cycloheximide (48 µM) was used as

736 a positive control. Translation inhibition (TI) percentage is calculated using this formula TI % =
737 (1− a/b) x 100, where 'a' equals the translation level with peptide and 'b' equals the translation
738 level without peptide.

739 ***In planta* and Semi-*In planta* antifungal assays**

740 Pepper (*Capsicum annuum*, California Wonder 300 TMR) plants used in this study were grown in
741 a greenhouse for 4 weeks under 14 h light/10 h dark cycle. Tomato (*Solanum lycopersicum* cv.
742 Mountain Spring) plants were grown in a controlled environment growth chamber for 4 weeks,
743 under a 16 h light/ 8 h dark cycle. Semi-*in planta* antifungal activity of each peptide against *B.*
744 *cinerea* was determined using detached leaves of pepper. NCR13_PFV1 and NCR13_PFV2 were
745 tested at 6, 1.5, and 0.09 μM. Following incubation of 10 μL peptide with 10 μL of *B. cinerea*
746 spores (~$10^5$ spores/mL) under a humid environment for 48 h, the leaves were photographed in
747 white light. High-resolution fluorescence images were also taken using CropReporter
748 (PhenoVation). These images depicted the calculated Fv/Fm (maximum quantum yield of
749 photosystem II ) values of the diseased area affected by *B. cinerea* infection. Colors in the images
750 show five different classes ranging from class I to class V (0.000 to 0.700) depicting varying
751 degrees of tissue damage.

752 To test the curative antifungal activity of peptides against *B. cinerea*, 4-week-old pepper and
753 tomato plants were used. Plants were first sprayed with 1 mL of *B. cinerea* spores (about $5 \times 10^4$)
754 suspended in 1× SFM. After 8 h of *B. cinerea* challenge, 2 mL of NCR13_PFV1 or NCR13_PFV2
755 (3.0 and 1.5 μM) were sprayed per plant. Control plants were sprayed with 2 mL of water. All
756 plants were placed in a high humid environment for 72 h. Plants were imaged at 72 h after infection
757 in white light and high-resolution fluorescence images were taken using CropReporter
758 (PhenoVation). The quantification of plant health was carried out using the calculated Fv/Fm

759 (maximum quantum yield of photosystem II) images of the CropReporter showing the efficiency
760 of photosynthesis in false colors.
761 For the curative assay using pepper and tomato plants, the picture of the whole plants and detached
762 leaves were taken as described above. The disease symptoms on individual leaves of each plant,
763 were visually assessed in % of disease portion (disease severity) and on a rating scale of 0-5 where
764 each rank would represent the following proportion of diseased tissue per leaf : Scale 0: No obvious
765 signs/symptoms of disease, Scale 1: $0 > x \leq 20$ % diseased portion of leaf, Scale 2: $20 > x \leq 40$ %
766 diseased portion of leaf, Scale 3: $40 > x \leq 60$ % diseased portion of leaf, Scale 4: $60 > x \leq 80$ %
767 diseased portion of leaf, Scale 5: $80 > x \leq 100$ % diseased portion of leaf. Four plants were used
768 per treatment and for each plant the disease was assessed per leaf. Besides disease severity (DS),
769 the inhibition of disease by treatment was also evaluated. The following formula was used to assess
770 the inhibition of disease severity by each treatment: % Disease Inhibition= (Average DS for
771 Control -Treatment DS)/(Average DS for Control ) x 100%. Where treatment DS is the disease
772 severity for each leaf except those of the control. Plots were generated using the 'ggplot2' package
773 in R version 4.3.2.

774 **Acknowledgements**

775 The work presented here was supported by the National Science Foundation grant IOS-2037981
776 and the National Institute of Food and Agriculture GRANT13515963 to D.S and K.C. The
777 structures for NCR13 were solved using resources at the W.R. Wiley Environmental Molecular
778 Sciences Laboratory, a national scientific user facility sponsored by U.S. Department of Energy's
779 Office of Biological and Environmental Research (BER) program located at Pacific Northwest
780 National Laboratory (PNNL). Battelle operates PNNL for the U.S. Department of Energy. We also
781 acknowledge imaging support from the Advanced Bioimaging Laboratory (RRID:SCR_018951) at

the Donald Danforth Plant Science Center (DDPSC) and usage of the Leica SPX-8 acquired through an NSF Major Research Instrumentation grant (DBI-1337680). The Washington University undergraduate summer intern Bram Osterhout contributed to the early work on NCR13 peptide. We also thank Dr. Ruby Tiwari for providing her comments on this manuscript. We acknowledge the DDPSC Proteomics & Mass Spectrometry Facility and supported by the National Science Foundation under Grant No. DBI-1827534 for acquisition of the Orbitrap Fusion Lumos LC-MS/MS. The greenhouse and growth chamber space provided by the DDPSC Plant Growth Facility is acknowledged. We also thank Dr. Ruby Tiwari for providing her comments on this manuscript.

**Author Contributions**

K.C., G.B. and D.S. conceived the research. J.G., A.D-C., S.V., M.T., K.C., M.Z., G.B. and D.S. designed the research. J.G., A.D-C., S.V., M.T., A.P., R.K, M.Z. and G.B. conducted the experiments. J.G., A.D-C., S.V., M.T., K.C., M.Z., G.B. and D.S. analyzed and interpreted the results. J.G., G.B., K.C. and D.S. wrote the manuscript.

**Competing interests**. The authors declare no competing interests.

**Data deposition**: The coordinates of the NCR13 NMR structure have been deposited in the Protein Data Bank, www.rcsb.org 8ULM (NCR13_ PFV1) and 7TH8 (NCR13_ PFV2) and the NMR chemical shifts have been deposited in the BioMagResBank, www.bmrb.wisc.edu BMRB-31111 (oxidized NCR13_PFV1) and BMRB-30979 (oxidized NCR13_PFV2).

806

807

808

809

810

811

812

813

814

A

```
CaNCR13  -TKPCQSDKDCKKFACRKPKVPKCINGFCKCVR-  32
CaNCR15  TKQPCKSRKHCKTYRCPTPKVPNCVNGFCKCVR-  33
CaNCR07  KKMPCKRRRDCKTYPCPHPKVRDCVKGYCKCVVR  34
```

B

| Peptide | Net Charge | % Hydrophobic amino acids | Predicted MW (kDa) | Isoelectric point | % identity with NCR13 |
|---|---|---|---|---|---|
| CaNCR13 | +8 | 28.1 | 3.66 | 9.59 | 100 |
| CaNCR15 | +9 | 24.2 | 3.81 | 9.82 | 66.6 |
| CaNCR07 | +10 | 26.5 | 4.08 | 9.85 | 48.4 |

C

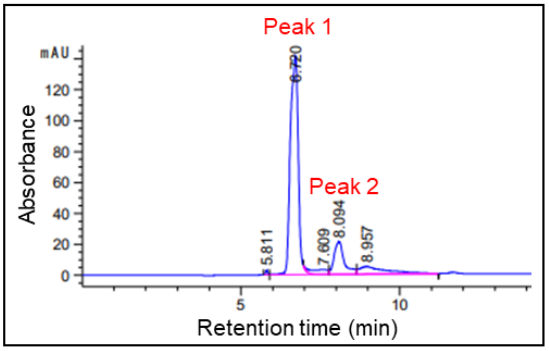


D

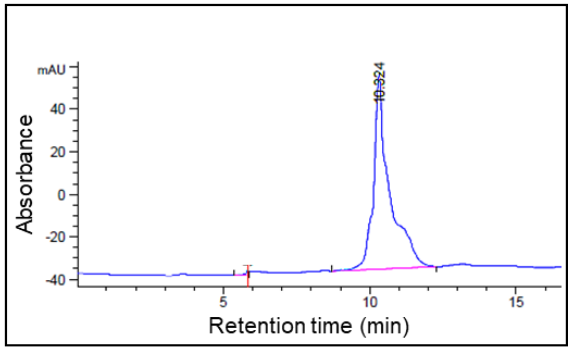


815

816 **Figure 1. Primary amino acid sequence and properties of NCR13.** (A) Primary amino acid
817 sequences for Chickpea (*C. arientinum*) NCR13 and its homologs NCR15 and NCR07. Conserved

818 cysteine residues are highlighted in red. The number of amino acids is indicated at the end of each
819 sequence. (B) Peptide characteristics of CaNCR13, CaNCR15 and CaNCR07. (C) High-
820 performance liquid chromatography (HPLC) analyses of NCR13 produced recombinantly in
821 *Pichia pastoris*, monitored at 260 nm, reveals the presence of two major products. mAU represents
822 milli-Absorbing Units. (D) Chemically synthesized NCR13 elutes as one HPLC peak.
823

824

825

826

827

828

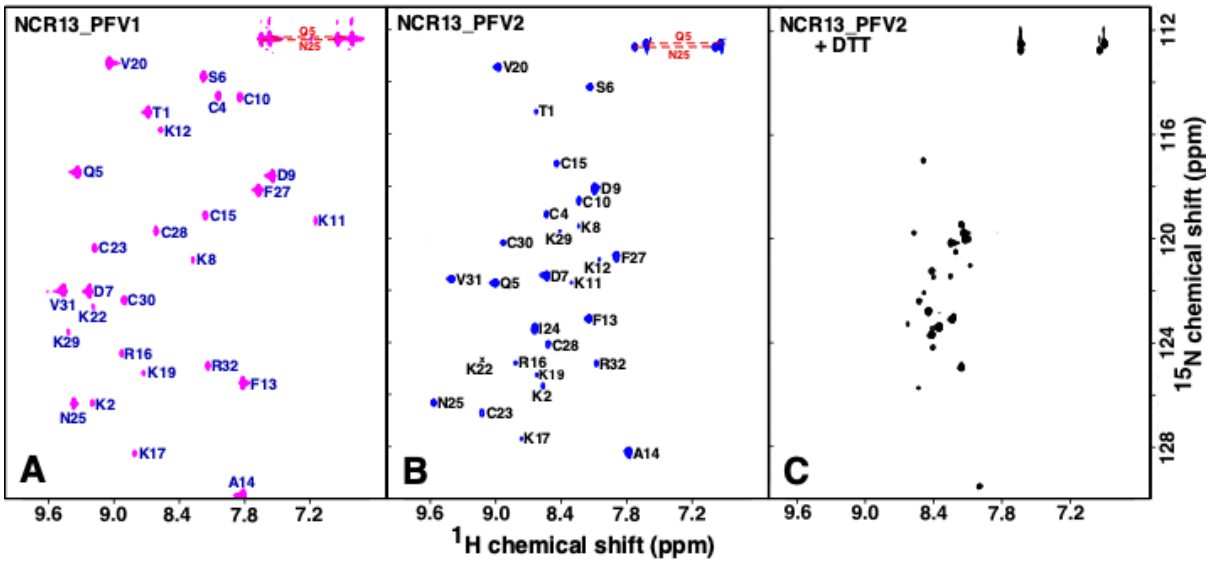

829

830 **Figure 2. Fingerprint $^{1}$H-$^{15}$N HSQC spectra for oxidized and reduced NCR13.** Assigned $^{1}$H-
831 $^{15}$N HSQC spectra for oxidized (disulfide) NCR13_PFV1 (A) and NCR13_PFV2 (B). (C) The $^{1}$H-
832 $^{15}$N HSQC spectrum of fully reduced (dithiol) NCR13_PFV1 and NCR13_PFV2 were identical
833 (the spectrum for NCR13_PFV2 is illustrated). All spectra collected on ~ 1 mM samples at 20°C
834 in 20 mM sodium acetate, 50 mM NaCl, pH 5.3 at a $^{1}$H resonance frequency of 600 MHz. Amide
835 side chain resonance pairs are connected by a red dashed line. Not within the displayed spectral
836 boundaries is the G26 amide resonance for NCR13_PFV1 and NCR13_PFV2 at 8.66/103.1 ppm
837 and 7.99/101.7 ppm, respectively, and the I24 amide resonance for NCR13_PFV1 at 8.72/132.0
838 ppm.
839

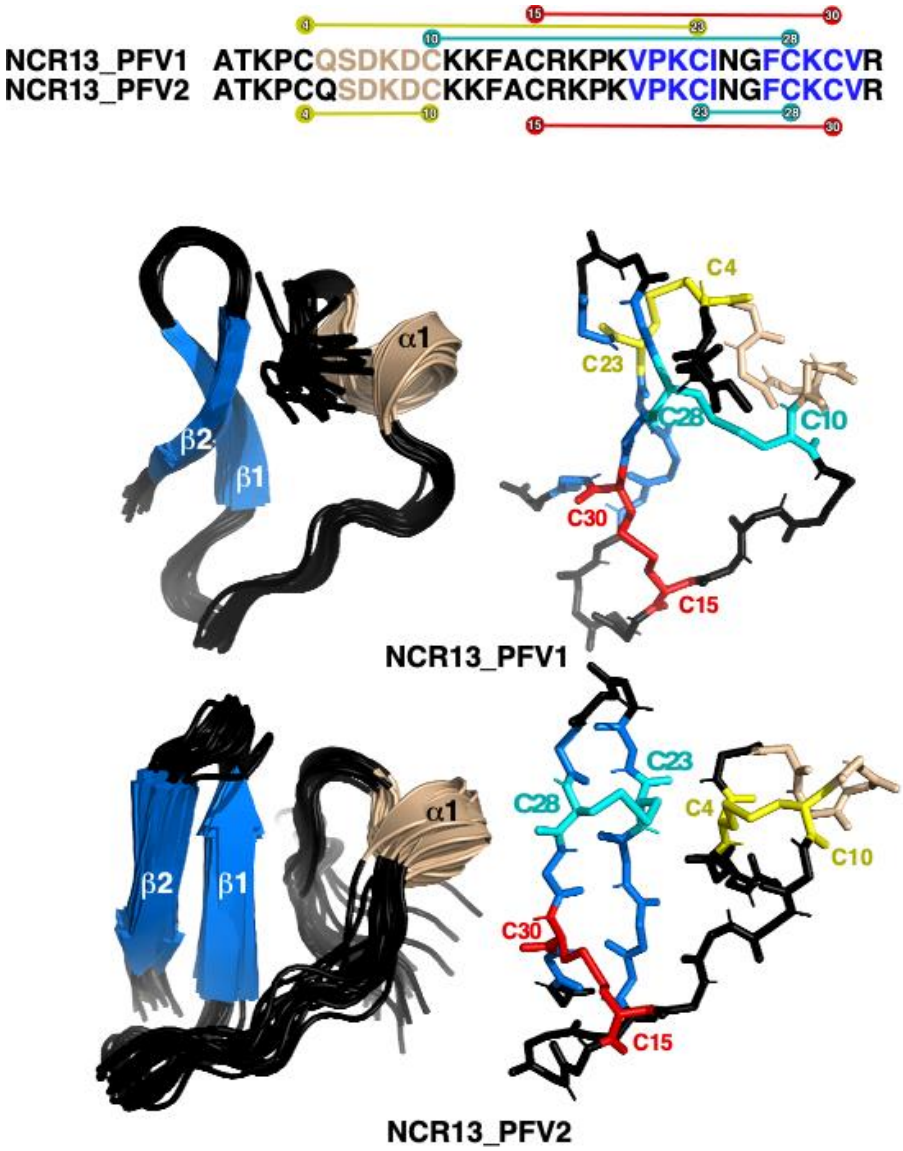


**Figure 3. Three-Dimensional NMR solution structure of NCR13_PFV1 and NCR13_PFV2.** Cartoon representation of the backbone superposition of the ordered regions in the ensemble of 20 structures calculated for oxidized NCR13_PFV1 (8ULM) and NCR13_PFV2 (7TH8). β-strands are colored blue and labeled sequentially starting from the N-terminal and the lone α-helix is colored wheat. Next to each ensemble is a backbone stick representation of a single structure with the six oxidized cysteine side chains highlighted in yellow, red, or cyan. Above the structures is a schematic summary of the elements of secondary structure observed for the two NMR structures, color-coded similarly. Also shown in the schematic are the disulfide bond connections in both isomers. One disulfide bond, between C15 and C30 (red), is identical in both isomers with C10 and C28 swapping disulfide bond partners.

A

| | 4 10 15 23 28 30 |
|---|---|
| NCR13 | TKP**C**QSDKD**C**KKFA**C**RKPKVPK**C**INGF**C**K**C**VR |
| NCR13_C4S-C23S | TKP**S**QSDKDCKKFACRKPKVPK**S**INGFCKCVR |
| NCR13_C10S-C28S | TKPCQSDKD**S**KKFACRKPKVPKCINGF**S**KCVR |
| NCR13_C15S-C30S | TKPCQSDKDCKKFA**S**RKPKVPKCINGFCK**S**VR |
| NSR13 | TKP**S**QSDKD**S**KKFA**S**RKPKVPK**S**INGF**S**K**S**VR |

B

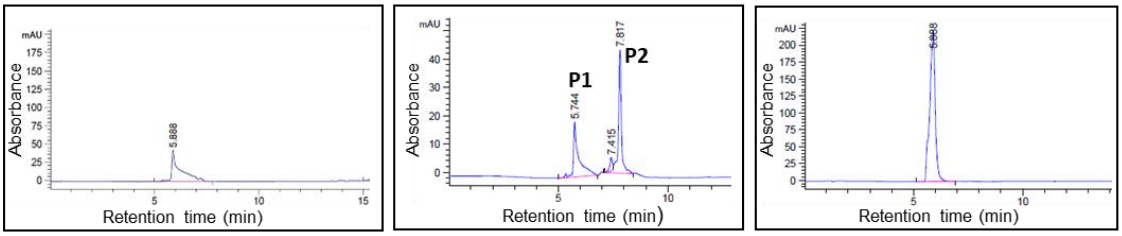


C

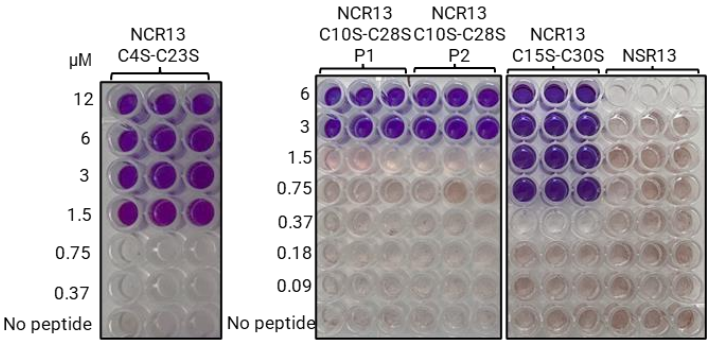


D

| Peptide Name | MIC (μM) |
|---|---|
| NCR13_PFV1 | 0.09 |
| NCR13_C4S-C23S | 1.5 |
| NCR13_C10S-C28S P1 | 3 |
| NCR13_C10S-C28S P2 | 3 |
| NCR13_C15S-C30S | 0.75 |
| NSR13 | Inactive |

**Figure 5. Removing disulfide bonds in NCR13_PFV1 reduces antifungal activity against *B. cinerea in vitro*.** (A) Four NCR13 constructs are used to assay the importance of disulfide bond formation for antifungal activity by substituting pairs of Cys residues with Ser (highlighted in red). The numbers above the sequence indicate the position of the Cys substitution. (B) HPLC analyses of NCR13_C4S-C23S, NCR13_C10S-C28S, and NCR13_C15S-C30S recombinantly produced in *P. pastoris* monitored at 260 nm (mAU = milli-Absorbing Units). (C) Fungal cell viability assay of disulfide knockout variants. A color change from blue to pink/clear indicative of metabolically active (live) *B. cinerea* germlings after 60 h. (D) Summary of the MIC values for NCR13_PFV1 and NCR13 disulfide knockout variants.

A

| Peptide | Sequence | MIC (μM) |
|---|---|---|
| NCR13_CS | TKPCQSDKDCKKFACRKPKVPKCINGFCKCVR | 3 |
| NCR13_AlaV1 | TKPC**AAAAA**CKKFACRKPKVPKCINGFCKCVR | 6 |
| NCR13_AlaV2 | TKPCQSDKDC**AAAA**CRKPKVPKCINGFCKCVR | Inactive (>12) |
| NCR13_AlaV3 | TKPCQSDKDCKKFAC**AAAA**VPKCINGFCKCVR | Inactive (>12) |
| NCR13_AlaV4 | TKPCQSDKDCKKFACRKPK**AAA**CINGFCKCVR | Inactive (>12) |
| NCR13_AlaV5 | TKPCQSDKDCKKFACRKPKVPKC**AAAA**CKCVR | 12 |

B

**Figure 6. Active motif of NCR13 required for antifungal activity.** (A) Antifungal activity of NCR13 synthetic peptide and NCR13 alanine variants against *B. cinerea*. Alanine scanning mutagenesis was done by substituting alanine within the NCR13 core sequence, leading to the creation of the NCR13_AlaV1-V5. MIC values were determined against *B. cinerea*. The amino acid substitutions are shown in red. Representative pictures are shown in Fig. *S5*. (B) Active motif of NCR13 (highlighted with a bold red font) required for its antifungal activity against *B. cinerea.* The secondary structure elements are shown above the amino acid sequence. The gray line and green arrow indicate α-helix (α1) and β-strand (β1) respectively.

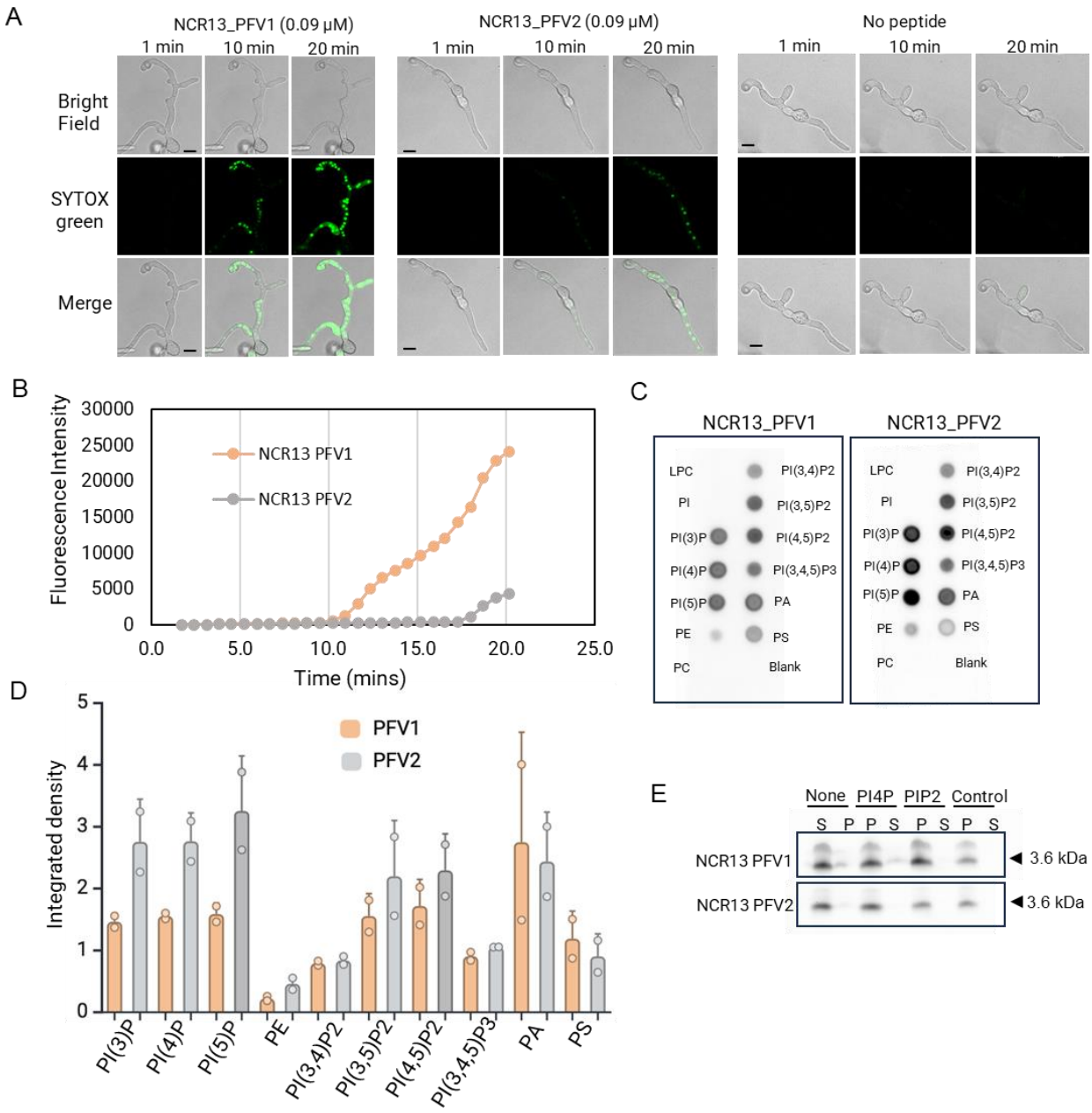


**Figure 7. NCR13 PFV1 permeabilizes the cell membrane of *B. cinerea* rapidly.** (A) Confocal microscopy images of SYTOX Green (SG) uptake in *B. cinerea* germlings at different time points. Germlings were treated with 0.09 μM NCR13_PFVs and SG dye simultaneously for 20 min. No peptide is used as a control. Scale bars = 10 μm. The experiment was repeated thrice with similar results. (B) Quantitative measurements of average fluorescence intensity over time to assess cell membrane permeability in *B. cinerea* germlings treated with 0.09 μM NCR13 PFVs. (C) PIP strip showing binding of NCR13 PFVs to multiple phospholipids, including phosphatidylinositol 4,5-bisphosphate ($PI(4,5)P_2$), phosphatidylinositol (3,4,5)-trisphosphate $PI(3,4,5)P_3$ and phosphatidylinositol monophosphates PI(3)P, PI(4)P, and PI(5)P, phosphatidylinositol

904 bisphosphate PI(3,4)$P_2$. (D) Integrated density measurement of PIP strip probed with
905 NCR13_PFVs. Datapoints are means ± SE of two independent biological replicates ($N = 2$). (E)
906 Binding of NCR13_PFVs to PI(4)P and PI(4,5)P2 ($PIP_2$) containing liposomes. NCR13_PFV's
907 were incubated without liposomes (None) and liposomes bearing no phosphoinositides (control),
908 S- supernatant fraction and P- pellet fraction.
909
910
911
912
913
914
915
916
917
918
919
920
921
922
923
924
925
926
927

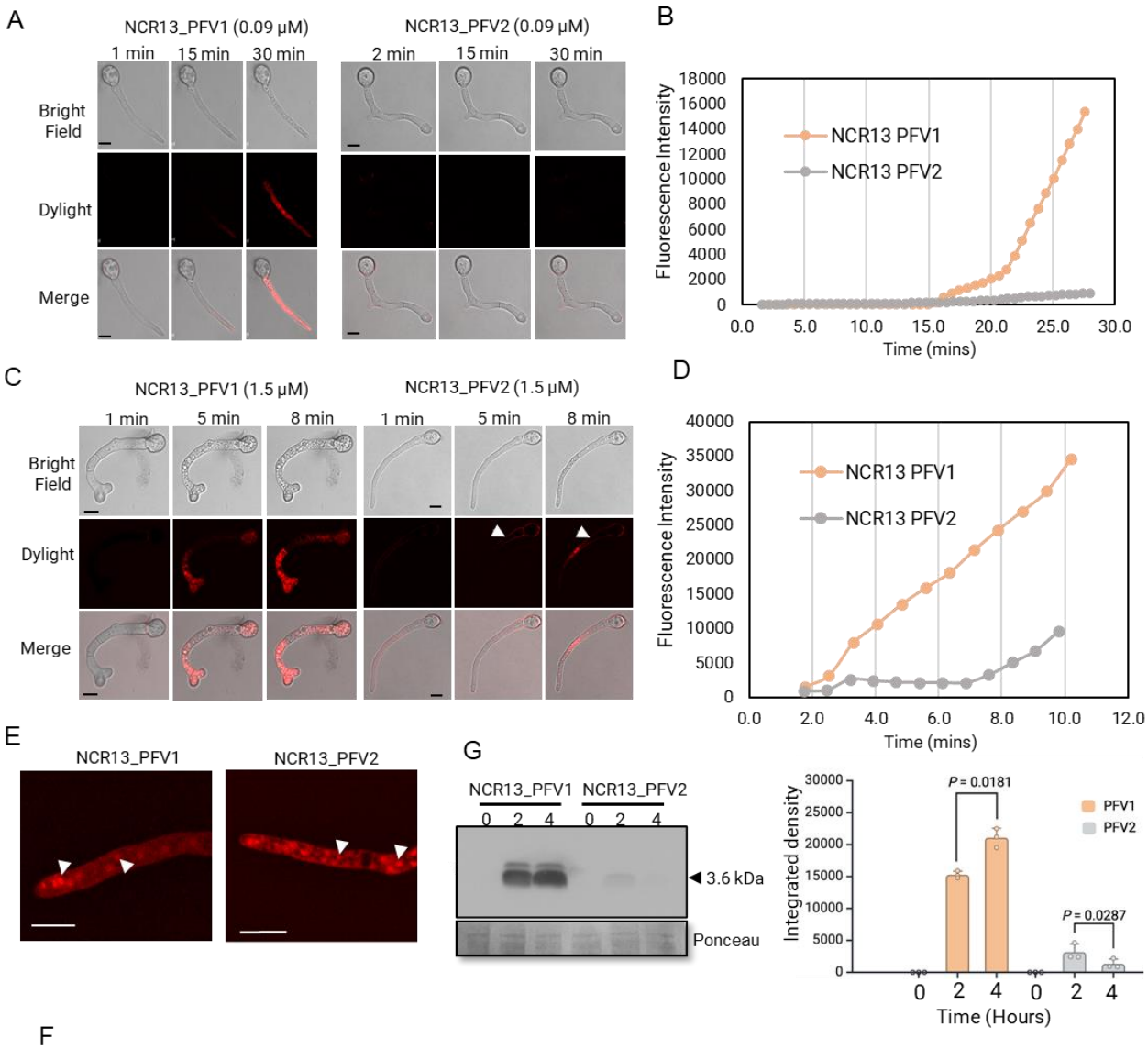
A
NCR13_PFV1 (0.09 μM)
1 min
15 min
30 min
NCR13_PFV2 (0.09 μM)
2 min
15 min
30 min
Bright Field
Dylight
Merge
B
Fluorescence Intensity
NCR13 PFV1
NCR13 PFV2
Time (mins)
C
NCR13_PFV1 (1.5 μM)
1 min
5 min
8 min
NCR13_PFV2 (1.5 μM)
1 min
5 min
8 min
Bright Field
Dylight
Merge
D
Fluorescence Intensity
NCR13 PFV1
NCR13 PFV2
Time (mins)
E
NCR13_PFV1
NCR13_PFV2
G
NCR13_PFV1
NCR13_PFV2
0 2 4 0 2 4
3.6 kDa
Ponceau
Integrated density
P = 0.0181
P = 0.0287
PFV1
PFV2
Time (Hours)

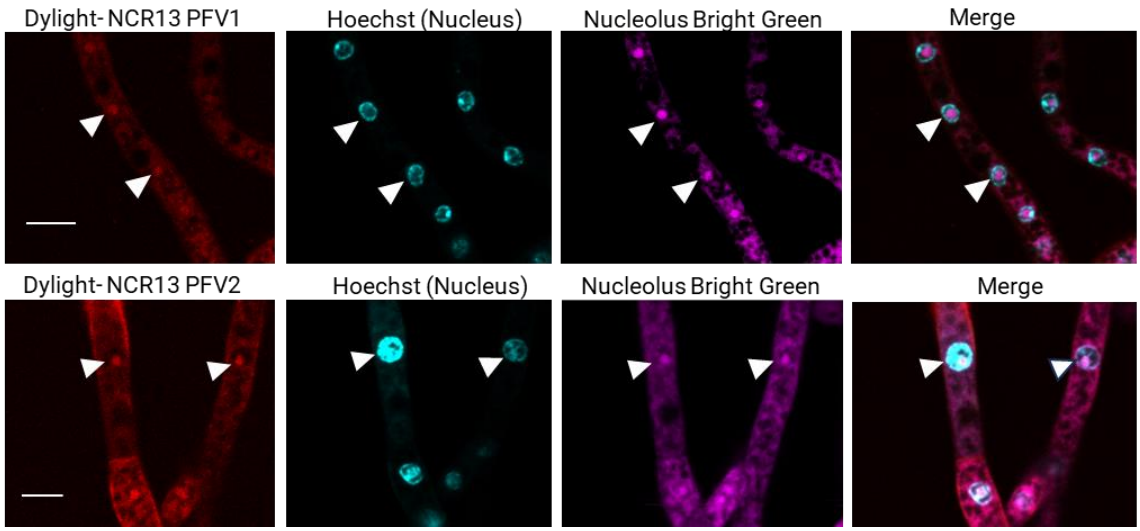
F
Dylight- NCR13 PFV1
Hoechst (Nucleus)
Nucleolus Bright Green
Merge
Dylight- NCR13 PFV2
Hoechst (Nucleus)
Nucleolus Bright Green
Merge

928

929 **Figure 8. Internalization and localization of NCR13 PFVs in *B. cinerea* germlings.** (A)
930 Confocal microscopy images of *B. cinerea* germlings at different points treated with 0.09 μM
931 DyLight550-labeled NCR13_PFV1 (left) and NCR_PFV2 (right) for 30 minutes. Scale bars = 10
932 μm. Data represents representative results of three independent experiments. (B) Quantification of
933 peptide internalization was conducted by analyzing the average fluorescence intensities over time
934 (in minutes) for NCR13_PFVs. The upper threshold for background was set at 23 for Fiji analysis.
935 (C) Confocal microscopy images of *B. cinerea* germlings treated with 1.5 μM DyLight550-labeled
936 NCR13_PFVs for 30 minutes. White arrowheads indicate NCR13_PFV2 on the cell surface. Scale
937 bars = 10 μm. (D) Quantitative measurements of peptide internalization in *B. cinerea* germlings
938 treated with 1.5 μM NCR13_PFV1 (left) and NCR13_PFV2 (right). (E) Internalized DyLight550-
939 labeled NCR13_PFV1 (left) and NCR13_PFV2 (right) concentrate in specific foci (white
940 arrowheads) within *B. cinerea* germlings. Scale bars = 10 μm. (F) NCR13_PFV1 and
941 NCR13_PFV2 localize to the nucleolus. DyLight550-labeled NCR13_PFV1 (upper panel) and
942 PFV2 (lower panel) colocalize with rRNA-specific Nucleolus Bright Green stain. Hoechst 33258
943 is used for staining nucleus. White arrowheads indicate nucleolar localization. Scale bars = 5 μm.
944 (G) Semi-quantitative analysis of NCR13_PFVs within *B. cinerea* germlings. Germlings were
945 treated with 1.5 μM NCR13_PFV1 and NCR13_PFV2 for 0, 2, and 4 hours. Total proteins were
946 extracted from fungal cells and immunoblotted using anti-NCR13 antibody. Equal loading of
947 proteins was verified using Ponceau staining. The bar graph represents integrated density
948 measurements. Statistical significance was tested using paired student's t-test. Data are shown as
949 mean ± SD (N = 3, where N refers to biological replicates).

950

951

952

953

954

955

956

957

958

959

960

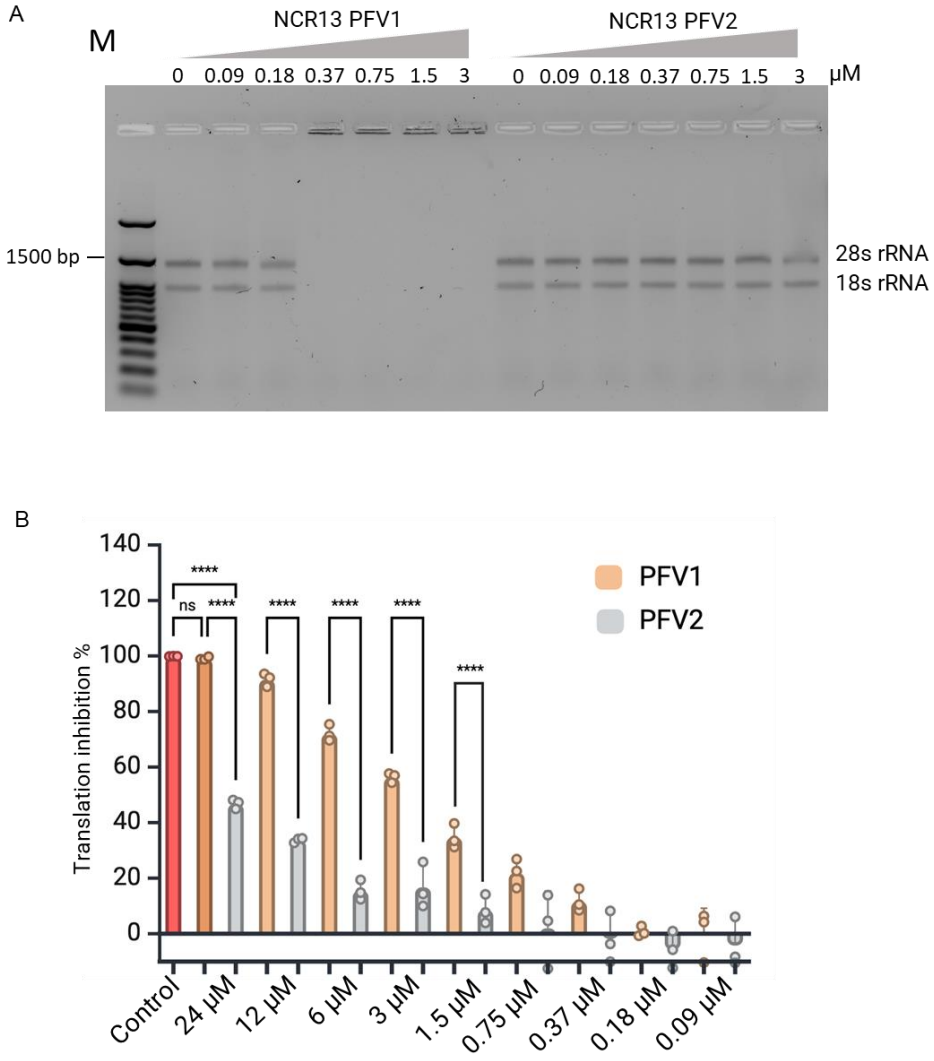


**Figure 9. NCR13_PFV1 exhibits rRNA binding and higher translation inhibition activity.** (A) rRNA binding by NCR13_PFVs tested using electrophoretic mobility shift assay (EMSA). *Botrytis cinerea* rRNA was used to assess the binding activity of the peptides NCR13_PFV1 and NCR13_PFV2. The binding reactions were subjected to electrophoresis, and the mobility shifts were visualized on an agarose gel (1%). The concentration gradient of peptides is indicated above the lanes. The first lane on the left contains a molecular weight marker. (B) Relative *in vitro* translational inhibition (%) in the presence of NCR13_PFVs at different concentrations. Sterile water was used as negative control and cycloheximide (96 μM) was used as positive control. N= 3, 'N' indicates biological replicates. Statistical significance is determined using One-way ANOVA with Tukey multiple comparisons test (**** indicates p value < 0.0001).

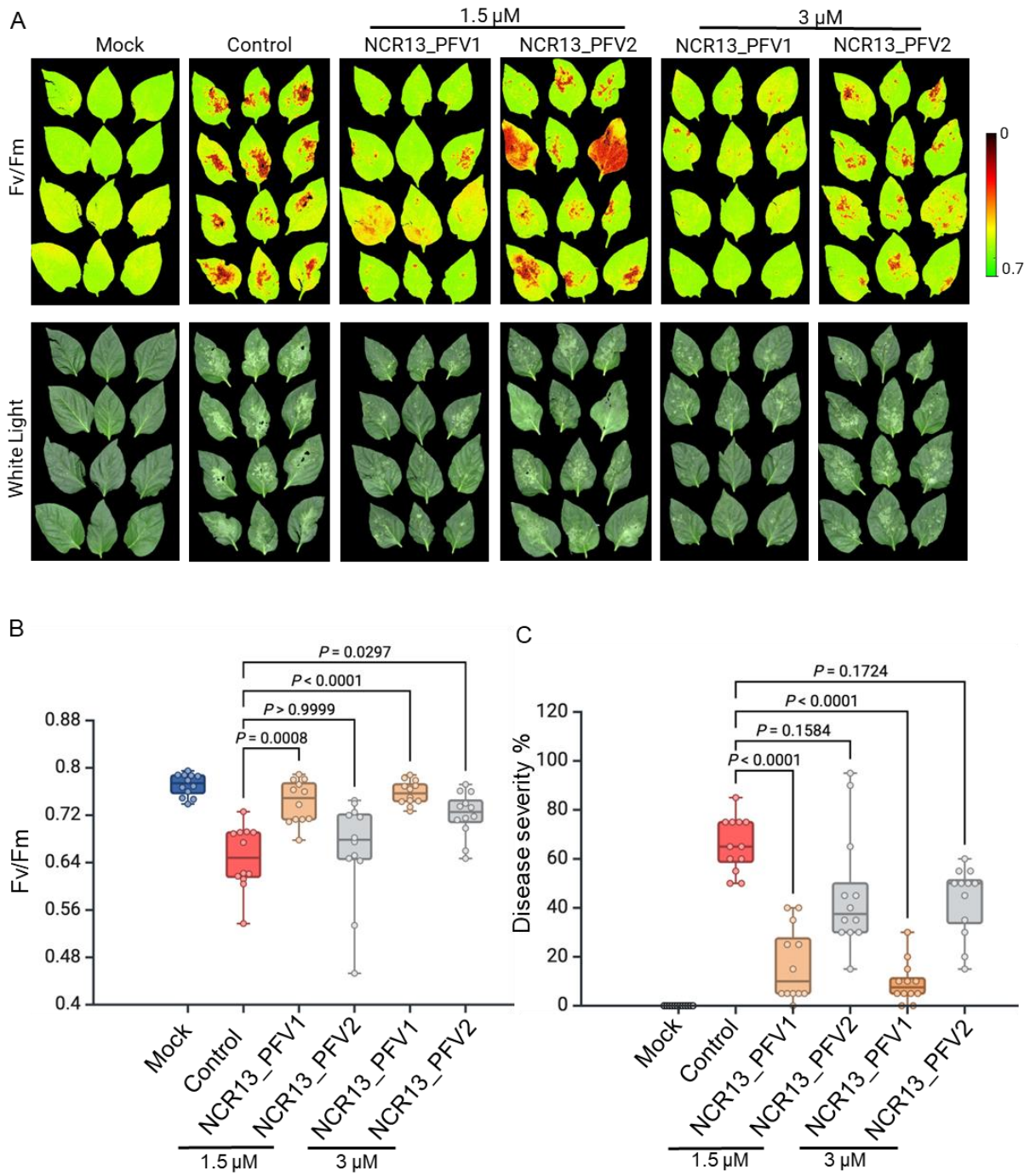


**Figure 10. NCR13 PFV1 exhibits enhanced curative antifungal activity against gray mold in pepper (*Capsicum annuum*) plants.** (A) Curative antifungal activity of NCR13_PFV1 and PFV2. Four-week-old pepper plants were first spray-inoculated using 1 mL of $5 \times 10^4$ *B. cinerea* spores. At 8 hpi (hours post inoculation), the plants were sprayed with 2 mL of peptide (NCR13_PFV1 or PFV2) at a concentration of 1.5 or 3 μM or control (*B. cinerea* alone). Mock-treated plants were only sprayed with 1X SFM (no fungal spore suspension). (B) Calculated photosynthetic quantum yield (Fv/Fm) for individual pepper plants. (C) Disease severity (%) was calculated as described

983 in materials and methods. (B-C) Each data point represents the average of 4 leaves per plant for 4
984 plants for each treatment. Horizontal lines represent the median and boxes indicate the 25th and
985 75th percentiles. The Kruskal-Wallis test with Dunn's multiple comparisons test is used to
986 determine statistically significant differences between control and peptide-treated inoculated
987 plants. Two independent experiments were performed with similar results.
988
989
990
991
992
993
994
995
996
997
998
999
1000
1001
1002
1003
1004
1005
1006
1007
1008

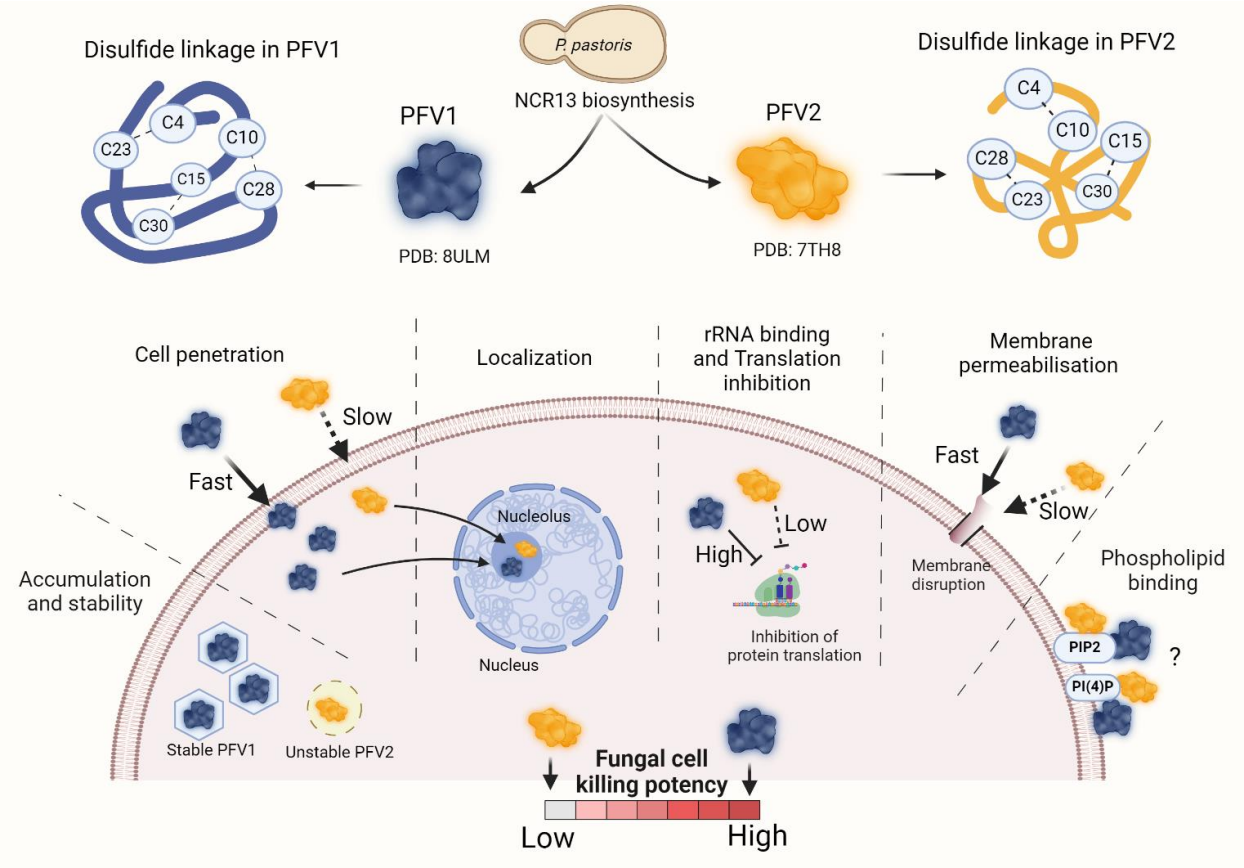


**Figure 11.** Graphical abstract illustrating the biosynthesis of disulfide linkage variants of NCR13_PFV1 and NCR13_PFV2 in *P. pastoris*, their structures and their effects on antifungal activity and modes of action in *B. cinerea* germlings. The figure depicts the differences in cell penetration, localization, rRNA binding and translation inhibition, membrane permeabilization, phospholipid binding, and overall fungal cell killing potency. Created using BioRender.com.

## References


Alhhazmi, A. A., Alluhibi, S. S., Alhujaily, R., Alenazi, M. E., Aljohani, T. L., Al-Jazzar, A. A., Aljabri, A. D., Albaqami, R., Almutairi, D., Alhelali, L. K., Albasri, H. M., Almutawif, Y. A., Alturkostani, M. A., & Almutairi, A. Z. (2024). Novel antimicrobial peptides identified in legume plant, Medicago truncatula. *Microbiol Spectr*, *12*(2), e0182723. https://doi.org/10.1128/spectrum.01827-23

Balogh, E. P., Mosolygo, T., Tiricz, H., Szabo, A. M., Karai, A., Kerekes, F., Virok, D. P., Kondorosi, E., & Burian, K. (2014). Anti-chlamydial effect of plant peptides. *Acta Microbiol Immunol Hung*, *61*(2), 229-239. https://doi.org/10.1556/AMicr.61.2014.2.12

Bhardwaj, G., Mulligan, V. K., Bahl, C. D., Gilmore, J. M., Harvey, P. J., Cheneval, O., Buchko, G. W., Pulavarti, S. V., Kaas, Q., Eletsky, A., Huang, P. S., Johnsen, W. A., Greisen, P. J., Rocklin, G. J., Song, Y., Linsky, T. W., Watkins, A., Rettie, S. A., Xu, X.,...Baker, D. (2016). Accurate de novo design of hyperstable constrained peptides. *Nature*, *538*(7625), 329-335. https://doi.org/10.1038/nature19791

Bhattacharya, A., Tejero, R., & Montelione, G. T. (2007). Evaluating protein structures determined by structural genomics consortia. *Proteins*, *66*(4), 778-795. https://doi.org/10.1002/prot.21165

Buchko, G. W., Hewitt, S. N., Van Voorhis, W. C., & Myler, P. J. (2018). Solution NMR structures of oxidized and reduced Ehrlichia chaffeensis thioredoxin: NMR-invisible structure owing to backbone dynamics. *Acta Crystallogr F Struct Biol Commun*, *74*(Pt 1), 46-56. https://doi.org/10.1107/S2053230X1701799X

Buchko, G. W., Pulavarti, S., Ovchinnikov, V., Shaw, E. A., Rettie, S. A., Myler, P. J., Karplus, M., Szyperski, T., Baker, D., & Bahl, C. D. (2018). Cytosolic expression, solution structures, and molecular dynamics simulation of genetically encodable disulfide-rich de novo designed peptides. *Protein Sci*, *27*(9), 1611-1623. https://doi.org/10.1002/pro.3453

Bulleid, N. J., & Ellgaard, L. (2011). Multiple ways to make disulfides. *Trends Biochem Sci*, *36*(9), 485-492. https://doi.org/10.1016/j.tibs.2011.05.004

Chadha, S., & Kale, S. P. (2015). Simple fluorescence-based high throughput cell viability assay for filamentous fungi. *Lett Appl Microbiol*, *61*(3), 238-244. https://doi.org/10.1111/lam.12460

Cools, T. L., Struyfs, C., Cammue, B. P., & Thevissen, K. (2017). Antifungal plant defensins: increased insight in their mode of action as a basis for their use to combat fungal infections. *Future Microbiol*, *12*, 441-454. https://doi.org/10.2217/fmb-2016-0181

Djami-Tchatchou, A. T., Tetorya, M., Godwin, J., Codjoe, J. M., Li, H., & Shah, D. M. (2023). Small Cationic Cysteine-Rich Defensin-Derived Antifungal Peptide Controls White Mold in Soybean. *J Fungi (Basel)*, *9*(9). https://doi.org/10.3390/jof9090873

Dos Santos-Silva, C. A., Zupin, L., Oliveira-Lima, M., Vilela, L. M. B., Bezerra-Neto, J. P., Ferreira-Neto, J. R., Ferreira, J. D. C., de Oliveira-Silva, R. L., Pires, C. J., Aburjaile, F. F., de Oliveira, M. F., Kido, E. A., Crovella, S., & Benko-Iseppon, A. M. (2020). Plant Antimicrobial Peptides: State of the Art, In Silico Prediction and Perspectives in the Omics Era. *Bioinform Biol Insights*, *14*, 1177932220952739. https://doi.org/10.1177/1177932220952739

Farkas, A., Maroti, G., Durgo, H., Gyorgypal, Z., Lima, R. M., Medzihradszky, K. F., Kereszt, A., Mergaert, P., & Kondorosi, E. (2014). Medicago truncatula symbiotic peptide NCR247 contributes to bacteroid differentiation through multiple mechanisms. *Proc Natl Acad Sci U S A*, *111*(14), 5183-5188. https://doi.org/10.1073/pnas.1404169111

Farkas, A., Maroti, G., Kereszt, A., & Kondorosi, E. (2017). Comparative Analysis of the Bacterial Membrane Disruption Effect of Two Natural Plant Antimicrobial Peptides. *Front Microbiol*, *8*, 51. https://doi.org/10.3389/fmicb.2017.00051

1068 Goyal, R. K., & Mattoo, A. K. (2014). Multitasking antimicrobial peptides in plant development and
1069 host defense against biotic/abiotic stress. *Plant Sci*, *228*, 135-149.
1070 https://doi.org/10.1016/j.plantsci.2014.05.012
1071 Guntert, P. (2004). Automated NMR structure calculation with CYANA. *Methods Mol Biol*, *278*, 353-
1072 378. https://doi.org/10.1385/1-59259-809-9:353
1073 Haag, A. F., Kerscher, B., Dall'Angelo, S., Sani, M., Longhi, R., Baloban, M., Wilson, H. M., Mergaert,
1074 P., Zanda, M., & Ferguson, G. P. (2012). Role of cysteine residues and disulfide bonds in the
1075 activity of a legume root nodule-specific, cysteine-rich peptide. *J Biol Chem*, *287*(14),
1076 10791-10798. https://doi.org/10.1074/jbc.M111.311316
1077 Hawkins, N. J., & Fraaije, B. A. (2018). Fitness Penalties in the Evolution of Fungicide Resistance.
1078 *Annu Rev Phytopathol*, *56*, 339-360. https://doi.org/10.1146/annurev-phyto-080417-050012
1079 Hellman, L. M., & Fried, M. G. (2007). Electrophoretic mobility shift assay (EMSA) for detecting
1080 protein-nucleic acid interactions. *Nat Protoc*, *2*(8), 1849-1861.
1081 https://doi.org/10.1038/nprot.2007.249
1082 Isozumi, N., Masubuchi, Y., Imamura, T., Mori, M., Koga, H., & Ohki, S. (2021). Structure and
1083 antimicrobial activity of NCR169, a nodule-specific cysteine-rich peptide of Medicago
1084 truncatula. *Sci Rep*, *11*(1), 9923. https://doi.org/10.1038/s41598-021-89485-w
1085 Jumper, J., Evans, R., Pritzel, A., Green, T., Figurnov, M., Ronneberger, O., Tunyasuvunakool, K.,
1086 Bates, R., Zidek, A., Potapenko, A., Bridgland, A., Meyer, C., Kohl, S. A. A., Ballard, A. J.,
1087 Cowie, A., Romera-Paredes, B., Nikolov, S., Jain, R., Adler, J.,...Hassabis, D. (2021). Highly
1088 accurate protein structure prediction with AlphaFold. *Nature*, *596*(7873), 583-589.
1089 https://doi.org/10.1038/s41586-021-03819-2
1090 Karbalaei, M., Rezaee, S. A., & Farsiani, H. (2020). Pichia pastoris: A highly successful expression
1091 system for optimal synthesis of heterologous proteins. *J Cell Physiol*, *235*(9), 5867-5881.
1092 https://doi.org/10.1002/jcp.29583
1093 Kereszt, A., Mergaert, P., Montiel, J., Endre, G., & Kondorosi, E. (2018). Impact of Plant Peptides on
1094 Symbiotic Nodule Development and Functioning. *Front Plant Sci*, *9*, 1026.
1095 https://doi.org/10.3389/fpls.2018.01026
1096 Kondorosi, E., Mergaert, P., & Kereszt, A. (2013). A paradigm for endosymbiotic life: cell
1097 differentiation of Rhizobium bacteria provoked by host plant factors. *Annu Rev Microbiol*,
1098 *67*, 611-628. https://doi.org/10.1146/annurev-micro-092412-155630
1099 Kovaleva, V., Bukhteeva, I., Kit, O. Y., & Nesmelova, I. V. (2020). Plant Defensins from a Structural
1100 Perspective. *Int J Mol Sci*, *21*(15). https://doi.org/10.3390/ijms21155307
1101 Lee, W., Rahimi, M., Lee, Y., & Chiu, A. (2021). POKY: a software suite for multidimensional NMR and
1102 3D structure calculation of biomolecules. *Bioinformatics*, *37*(18), 3041-3042.
1103 https://doi.org/10.1093/bioinformatics/btab180
1104 Li, H., Kalunke, R., Tetorya, M., Czymmek, K. J., & Shah, D. M. (2024). Modes of action and potential
1105 as a peptide-based biofungicide of a plant defensin MtDef4. *Mol Plant Pathol*, *25, e134538*.
1106 *https://doi.org/10.1111/mpp.134538*.
1107 Li, H., Velivelli, S. L., & Shah, D. M. (2019). Antifungal potency and modes of action of a novel olive
1108 tree defensin against closely related ascomycete fungal pathogens. . *Mol Plant Microbe*
1109 *Interact*, *32*, 164901664. https://doi.org/10.1094/MPMI-08-19-0224-R
1110 Liang, J., Shah, D. M., Wu, Y., Rosenberger, C. A., & Hakimi, S. M. (2001). *Antifungal polypeptide*
1111 *from alfalfa and methods for controlling plant pathogenic fungi* (USA Patent No. US
1112 6316407).
1113 Lima, R. M., Kylarova, S., Mergaert, P., & Kondorosi, E. (2020). Unexplored Arsenals of Legume
1114 Peptides With Potential for Their Applications in Medicine and Agriculture. *Front Microbiol*,
1115 *11*, 1307. https://doi.org/10.3389/fmicb.2020.01307

Lobo, F., & Boto, A. (2022). Host-defense peptides as new generation phytosanitaries: Low toxicity and low induction of antimicrobial resistance. *Agronomy*, *12*, 1614. https://doi.org/https://doi.org/10.3390/agronomy12071614

Maroti, G., Downie, J. A., & Kondorosi, E. (2015). Plant cysteine-rich peptides that inhibit pathogen growth and control rhizobial differentiation in legume nodules. *Curr Opin Plant Biol*, *26*, 57-63. https://doi.org/10.1016/j.pbi.2015.05.031

McLaughlin, M. S., Roy, M., Abbasi, P. A., Carisse, O., Yurgel, S. N., & Ali, S. (2023). Why Do We Need Alternative Methods for Fungal Disease Management in Plants? *Plants (Basel)*, *12*(22). https://doi.org/10.3390/plants12223822

Mergaert, P. (2018). Role of antimicrobial peptides in controlling symbiotic bacterial populations. *Nat Prod Rep*, *35*(4), 336-356. https://doi.org/10.1039/c7np00056a

Montiel, J., Downie, J. A., Farkas, A., Bihari, P., Herczeg, R., Balint, B., Mergaert, P., Kereszt, A., & Kondorosi, E. (2017). Morphotype of bacteroids in different legumes correlates with the number and type of symbiotic NCR peptides. *Proc Natl Acad Sci U S A*, *114*(19), 5041-5046. https://doi.org/10.1073/pnas.1704217114

Montiel, J., Szucs, A., Boboescu, I. Z., Gherman, V. D., Kondorosi, E., & Kereszt, A. (2016). Terminal Bacteroid Differentiation Is Associated With Variable Morphological Changes in Legume Species Belonging to the Inverted Repeat-Lacking Clade. *Mol Plant Microbe Interact*, *29*(3), 210-219. https://doi.org/10.1094/MPMI-09-15-0213-R

Olliver, C. L., Grobler-Rabie, A., & Boyd, C. D. (1985). In vitro translation of messenger RNA in a wheat germ extract cell-free system. *Methods Mol Biol*, *2*, 137-144. https://doi.org/10.1385/0-89603-064-4:137

Ordogh, L., Voros, A., Nagy, I., Kondorosi, E., & Kereszt, A. (2014). Symbiotic plant peptides eliminate Candida albicans both in vitro and in an epithelial infection model and inhibit the proliferation of immortalized human cells. *Biomed Res Int*, *2014*, 320796. https://doi.org/10.1155/2014/320796

Parisi, K., Shafee, T. M. A., Quimbar, P., van der Weerden, N. L., Bleackley, M. R., & Anderson, M. A. (2019). The evolution, function and mechanisms of action for plant defensins. *Semin Cell Dev Biol*, *88*, 107-118. https://doi.org/10.1016/j.semcdb.2018.02.004

Poon, I., Baxter, A. A., Lay, F. T., Mills, G. D., Adda, C. G., Payne, J. A., Phan, T. K., Ryan, G. F., White, J. A., Veneer, P. K., van der Weerden, N. L., Anderson, M. A., Kvansakul, M., & Hulett, M. D. (2014). Phosphoinositide-mediated oligomerization of a defensin induces cell lysis. *Elife*, *3*, e01808. https://doi.org/10.7554/eLife.01808

Schindelin, J., Arganda-Carreras, I., Frise, E., Kaynig, V., Longair, M., Pietzsch, T., Preibisch, S., Rueden, C., Saalfeld, S., Schmid, B., Tinevez, J. Y., White, D. J., Hartenstein, V., Eliceiri, K., Tomancak, P., & Cardona, A. (2012). Fiji: an open-source platform for biological-image analysis. *Nat Methods*, *9*(7), 676-682. https://doi.org/10.1038/nmeth.2019

Shabab, M., Arnold, M. F., Penterman, J., Wommack, A. J., Bocker, H. T., Price, P. A., Griffitts, J. S., Nolan, E. M., & Walker, G. C. (2016). Disulfide cross-linking influences symbiotic activities of nodule peptide NCR247. *Proc Natl Acad Sci U S A*, *113*(36), 10157-10162. https://doi.org/10.1073/pnas.1610724113

Shaw, W. J., Tarasevich, B. J., Buchko, G. W., Arachchige, R. M. J., & Burton, S. D. (2020). Controls of nature: Secondary, tertiary, and quaternary structure of the enamel protein amelogenin in solution and on hydroxyapatite. *J Struct Biol*, *212*(3), 107630. https://doi.org/10.1016/j.jsb.2020.107630

Shen, Y., Delaglio, F., Cornilescu, G., & Bax, A. (2009). TALOS+: a hybrid method for predicting protein backbone torsion angles from NMR chemical shifts. *J Biomol NMR*, *44*(4), 213-223. https://doi.org/10.1007/s10858-009-9333-z

Tavormina, P., De Coninck, B., Nikonorova, N., De Smet, I., & Cammue, B. P. (2015). The Plant Peptidome: An Expanding Repertoire of Structural Features and Biological Functions. *Plant Cell*, *27*(8), 2095-2118. https://doi.org/10.1105/tpc.15.00440

Tiricz, H., Szűcs, A., Farkas, A., Pap, B., Lima, R. M., Maróti, G., Kondorosi, É., & Kereszt, A. (2013). Antimicrobial Nodule-Specific Cysteine-Rich Peptides Induce Membrane Depolarization-Associated Changes in the Transcriptome. *Applied and Environmental Microbiology*, *79*(21), 6737. https://doi.org/10.1128/AEM.01791-13

van der Weerden, N. L., Bleackley, M. R., & Anderson, M. A. (2013). Properties and mechanisms of action of naturally occurring antifungal peptides. *Cell Mol Life Sci*, *70*(19), 3545-3570. https://doi.org/10.1007/s00018-013-1260-1

Velivelli, S. L. S., Czymmek, K. J., Li, H., Shaw, J. B., Buchko, G. W., & Shah, D. M. (2020). Antifungal symbiotic peptide NCR044 exhibits unique structure and multifaceted mechanisms of action that confer plant protection. *Proc Natl Acad Sci U S A*, *117*(27), 16043-16054. https://doi.org/10.1073/pnas.2003526117

Wedemeyer, W. J., Welker, E., Narayan, M., & Scheraga, H. A. (2000). Disulfide bonds and protein folding. *Biochemistry*, *39*(23), 7032. https://doi.org/10.1021/bi005111p

Yee, A., Chang, X., Pineda-Lucena, A., Wu, B., Semesi, A., Le, B., Ramelot, T., Lee, G. M., Bhattacharyya, S., Gutierrez, P., Denisov, A., Lee, C. H., Cort, J. R., Kozlov, G., Liao, J., Finak, G., Chen, L., Wishart, D., Lee, W.,...Arrowsmith, C. H. (2002). An NMR approach to structural proteomics. *Proc Natl Acad Sci U S A*, *99*(4), 1825-1830. https://doi.org/10.1073/pnas.042684599